

Where and how the East Madagascar Current retroreflection originates?

Juliano D. Ramanantsoa^{1,2,3,11*}, P. Penven⁴, R. P. Raj⁵, L. Renault⁶, L. Ponsoni⁷, M. Ostrowski⁸, A. F. Dilmahamod^{9,10}, M. Rouault^{1,3}

¹Department of Oceanography, University of Cape Town (UCT), South Africa

²Norwegian Research Center (NORCE), Bergen, Norway

³Nansen Tutu for Marine Environmental Research, Ma-Re Institute, University of Cape Town (UCT),
South Africa

⁴Univ. Brest, CNRS, IRD, Ifremer, Laboratoire d'Océanographie Physique et Spatiale (LOPS), IUEM,
Brest, France

⁵Nansen Environmental and Remote Sensing Center (NERSC), Bjerknes Center for Climate Research
(BCCR), Bergen, Norway

⁶Department of Atmospheric and Oceanic Sciences, University of California, Los Angeles, Los Angeles,
California, and Laboratoire d'Étude en Géophysique et Océanographie Spatiale, IRD, Toulouse, France

⁷Georges Lemaître Centre for Earth and Climate Research (TECLIM), Earth and Life Institute,
Université catholique de Louvain, Louvain-la-Neuve, Belgium

⁸Institute of Marine Research (IMR), Bergen, Norway

⁹GEOMAR Helmholtz Centre for Ocean Research Kiel, Kiel, Germany

¹⁰Department of Oceanography, Dalhousie University, Halifax, Nova Scotia B3H 4R2, Canada

¹¹Institut Halieutique et des Sciences Marines (IH.SM), Toliara, Madagascar

Key Points:

- The East Madagascar Current (EMC) retroreflection is assessed. Evidence of EMC early retroreflection is demonstrated for the first time.
- Retroreflection regimes are associated with EMC strength and mesoscale variability.
- Knowledge of the EMC retroreflection state helps understand regional ecosystem variability.

*Department of Oceanography, University of Cape Town, office 123, Private Bag X3, Rondebosch 7701, Cape Town, South Africa

Corresponding author: Juliano Heriniaina Dani Ramanantsoa, oceanman1@live.fr

Abstract

The East Madagascar Current (EMC) is one of the western boundary currents of the South Indian Ocean. As such, it plays an important role in the climate system by transporting water and heat towards the pole and recirculating to the large-scale Indian Ocean through retroflection modes of its southern extension. Five cruise datasets and remote sensing data from different sensors are used to identify three states of the southern extension of the East Madagascar Current (EMC): early retroflection, canonical retroflection and no retroflection. Retroflections occur 47% of the time. EMC strength regulates the retroflection state, although impinged mesoscale eddies also contribute to retroflection formation. Early retroflection is linked with EMC volume transport. Anticyclonic eddies drifting from the central Indian Ocean to the coast favour early retroflection formation, anticyclonic eddies near the southern tip of Madagascar promote the generation of canonical retroflection, and no retroflection appears to be associated with a lower eddy kinetic energy (EKE). Knowledge of the EMC retroflection state could help predict (1) coastal upwelling south of Madagascar, (2) the southeastern Madagascar phytoplankton bloom, and (3) the formation of the South Indian Ocean Counter Current (SICC).

Plain Language Summary

Using in situ and satellite observations, we show that the East Madagascar Current (EMC), a strong current flowing along the East Coast of Madagascar, often detaches from the coast before the southern tip of the island and goes directly into the Indian Ocean, the so-called EMC retroflection. The EMC retroflection is characterized by three well-defined forms: early retroflection, canonical retroflection, and no retroflection. The EMC Early Retroflection is an unusual abrupt return current straight to the Indian Ocean without reaching the detachment point, while the EMC Canonical Retroflection returns the mass flow in the vicinity of the southern tip of the island. No retroflection is characterized by the straight propagation of the flow towards the Agulhas Current. These three forms of retroflection are due to the strength of the EMC and the contribution of mesoscale eddies arriving from the Indian Ocean. Retroflections have implications for coastal upwelling strength, Southeast Madagascar phytoplankton bloom occurrences, and South Indian Ocean Counter Current (SICC) formation.

58 1 Introduction

59 Due to the presence of Madagascar Island and the consequence of wind-driven cir-
 60 culation in the South Indian Ocean, a continuous western boundary current, the East
 61 Madagascar Current (EMC), is formed along the east coast of the island (J. Lutjeharms
 62 et al., 1981; Penven, Lutjeharms, & Florenchie, 2006). The South Equatorial Current
 63 (Figure 1b) flows from east to west in the South Indian Ocean near the Mascarene Plateau
 64 ($\sim 60^\circ\text{E}$) between 10°S and 20°S . It is mainly driven by southeasterly trade winds (Palastanga
 65 et al., 2006; Nauw et al., 2008). Upon reaching the western boundary of the east Mada-
 66 gascar coast, the South Equatorial Current bifurcates into the equatorward-flowing North
 67 Madagascar Current (Figure 1d) and poleward-flowing East Madagascar Current (Fig-
 68 ure 1c) (J. Lutjeharms, 1976; J. Swallow et al., 1988). The South Equatorial Current bi-
 69 furcation off the east Madagascar coast was documented to occur at approximately 17°S
 70 at the surface (J. Swallow et al., 1988) and at approximately 20°S at 800 - 900 m depth
 71 (Chapman et al., 2003). On average, the bifurcation of the southern branch of the South
 72 Equatorial Current takes place at 18°S , although Chen et al. (2014) observed an annual
 73 variability of approximately 1° , with the southernmost and northernmost bifurcation lo-
 74 cations taking place in June-July and November-December, respectively.

75 The EMC originates from that southward branch resulting from the South Equa-
 76 torial Current split after its separation near the east Madagascar continental margin. The
 77 EMC is a western boundary current flowing along the east coast of Madagascar and con-
 78 stitutes a major contributor to the Agulhas Current (Figure 1i) (Penven, Lutjeharms,
 79 & Florenchie, 2006), which plays a significant role in the return flow of the Atlantic Merid-
 80 ional Overturning Circulation (Talley, 2013). Observational in situ data show that the
 81 EMC flows primarily over the eastern Madagascar continental slope, with a mean core
 82 placed at the surface and approximately 20 km off the coast, with a width ranging be-
 83 tween 60 and 100 km (Ponsoni et al., 2016). Vertically, the EMC reaches an average depth
 84 of 1000 m, where there is a reversal of the flow that characterizes the transition to the
 85 equatorward-flowing East Madagascar Undercurrent (Ponsoni, Aguiar-González, et al.,
 86 2015). The EMC presents mean values of surface velocity on the order of $79 (\pm 21) \text{ cm}$
 87 s^{-1} and $18.3 (\pm 8.4) \text{ Sv}$ volume transport. However, the current is marked by a well-defined
 88 nearly bimonthly variability (45-85 days), which leads to strong events with maximum
 89 velocities and volume transports of up to 170 cm s^{-1} and 50 Sv (Ponsoni et al., 2016).
 90 As shown by a combination of in situ and satellite observations, the nearly bimonthly

91 variability explains approximately 41% of the EMC variance and is clearly forced by the
92 arrival of westward-propagating sea level anomalies (Ponsoni et al., 2016). These anoma-
93 lies might be perceived as mesoscale cyclonic and anticyclonic eddies. Upon arriving near
94 the Madagascar coast, the eddies interact with the EMC, which is intensified (attenu-
95 ated) by anticyclonic (cyclonic) features (Ponsoni et al., 2016). The strength of the EMC
96 also varies on interannual time scales, mostly related to the large-scale climate variabil-
97 ity over the Indian Ocean. The large-scale sea surface height (SSH) signals, related to
98 the occurrence of the Indian Ocean dipole (Saji et al., 1999), may interact with the Mada-
99 gascar coast at a lag of +1 year after each Indian Ocean dipole phase. The positive phase
100 of the Indian Ocean dipole is associated with positive SSH anomalies in the tropical In-
101 dian Ocean, which tend to decrease circulation in both tropical and northward exten-
102 sions of the subtropical gyre. During negative phases of the Indian Ocean Dipole, an in-
103 tensification of the EMC was observed, pointing to a strengthening and/or southward
104 extension of the tropical gyre related to the Indian Ocean Dipole-induced negative SSH
105 (Palastanga et al., 2006).

106 Before propagating towards the Agulhas Current, the southern extension of the EMC
107 is also perceived to flow eastward and to act as a feeder of the South Indian Ocean Coun-
108 tercurrent (SICC) (Figure 11) (J. Lutjeharms, 1988; Siedler et al., 2006; Palastanga et
109 al., 2006). Pairing oceanographic cruise data and satellite observations, J. Lutjeharms
110 et al. (1981) and J. Lutjeharms (1988) found that the southern extension of the EMC
111 had a return current. Later, using satellite data and the OCCAM numerical model (Ocean
112 Circulation and Climate Advanced Modeling; Gwilliam et al. (1997); Saunders et al. (1999)),
113 the concept of the EMC retroflection was reconsidered by Quartly et al. (2006). The se-
114 quences of satellite images agreed well with the model output, showing an intermittence
115 of anticyclonic eddies moving westward, which seemed to affect the EMC retroflection.
116 Siedler et al. (2009) demonstrated that the southern extension of the EMC has two states:
117 the first is the state of no retroflection characterized by the flow directly contributing
118 to the total volume transport of the Agulhas Current; and the second state is a retroflec-
119 tion where most of the flow returns back directly to the South Indian Ocean via the SICC.
120 They found the existence of a variable retroflection with a significant proportion of the
121 EMC flowing towards the Agulhas Current and almost half propagating into the SICC.
122 Numerical models have difficulties simulating retroflection dynamics. In most modelling
123 work in the region, based on ROMS (Regional Ocean Modeling System; Penven, Debreu,

124 et al. (2006)), HYCOM (Hybrid-Coordinate Ocean Model; Chassignet et al. (2007)), HIM
125 (Hallberg Isopycnal Model; Lambert et al. (2016)), and NEMO (Nucleus for European
126 Modelling of the Ocean), the location of the eastward-flowing SICC does not seem to cor-
127 relate well compared to altimetry data. It is shifted 1-2° north, which cannot accurately
128 simulate the dynamics of the retroflexion (see Figure 4 in Lambert et al. (2016); Fig-
129 ure 5 in Siedler et al. (2009); Figure 2 in Halo et al. (2014)). Halo et al. (2014) and Jose
130 et al. (2016) simulated eddy activities south of Mozambique and southwest of Madagas-
131 car. Both simulations explained the complex role of mesoscale eddy processes driving
132 offshore propagation of water from the EMC through the dipole of eddies south of Mada-
133 gascar.

134 The characteristics of retroflexion and their mechanical drivers are still unknown.
135 Few studies have accurately addressed the retroflexion types or their formations. Siedler
136 et al. (2009) suggested that the EMC holds two different modes, which change from one
137 regime to the other, depending on the intensity of the EMC. The first mode is a west-
138 ward flow after rounding the southern tip of Madagascar, which is induced by a cyclonic
139 motion owing to friction with the inshore edge (de Ruijter et al., 2004). The second mode
140 is an anticyclonic motion, owing to the southwestward flow of the EMC and hence to the
141 absence of frictional effects with the slope. The planetary vorticity changes result in an
142 anticyclonic motion to conserve absolute vorticity. This favours a retroflexion to the east
143 and northeast. Halo et al. (2014) indicated that the connection between the EMC and
144 a retroflexion could be established through the shedding of anticyclonic eddies, hence
145 consistent with a nonpersistent retroflexion of the EMC, as stated by Quartly et al. (2006).
146 de Ruijter et al. (2004) and Palastanga et al. (2007) added that the unclear interactions
147 of the westward-propagating mesoscale eddies drifted from the Indian Ocean between
148 20°S and 30°S with the mean flow of the EMC appearing to initiate the formation of the
149 retroflexion. However, Ou and De Ruijter (1986) and Arruda et al. (2014) were the few
150 studies suggesting a theoretical explanation of the retroflexion in the South Indian Ocean.
151 Ou and De Ruijter (1986) investigated the key processes responsible for the Agulhas Cur-
152 rent retroflexion. Using one- and half-layer models, they explained the formation of a
153 meander initiating retroflexion due to the interaction between the Agulhas Current in-
154 tensity and the continental margin. Arruda et al. (2014) suggested that the increase of
155 the basic eddy volume associated with variation of β -effect and the net mass flux going
156 into the eddies explained the Agulhas Current retroflexion dynamics from an analyt-

157 ical model satisfying the mass conservation, the momentum balance, and the time-dependent
158 equation. Both studies converge to suggest that potential vorticity balance variation is
159 associated with the generation of retroflection for the Agulhas Current case, which may
160 also be replicated for the EMC case.

161 EMC retroflection has recently gained interest in the scientific community because
162 of its possible link with the Southeast Madagascar Bloom (Dilmahamod et al., 2019),
163 with coastal upwelling in southern Madagascar (Ramanantsoa et al., 2018a), and its in-
164 fluence on Agulhas Current variability (J. Lutjeharms et al., 1981). Previous studies have
165 documented that EMC retroflection transports nutrient-rich waters, triggering this mas-
166 sive phytoplankton bloom to expand towards the central Indian Ocean (Longhurst, 2001;
167 R. P. Raj et al., 2010). The EMC southern extension behaviour is also known to influ-
168 ence coastal upwelling at the southern tip of Madagascar (Ho et al., 2004; Ramanantsoa
169 et al., 2018a), which has implications for local biological productivity (Bemiasa, 2009).
170 The impact of the retroflection on coastal upwelling and on the transport of nutrients
171 into the region of the bloom is unknown.

172 The Indian Ocean has recently been described as the fastest-warming ocean in the
173 world for the last two decades (Hu & Fedorov, 2019; Rao et al., 2012). The western bound-
174 ary currents in this ocean, such as the EMC, play a key role in transporting heat from
175 the tropics towards the poles (Hastenrath, 2000; Sheppard, 2003; Deo et al., 2011). In
176 that case, the EMC is a central location connecting the Agulhas Current and the cen-
177 tral Indian Ocean. There is a crucial need to assess the functioning of the EMC to suc-
178 cessfully establish the connection between tropical and/or subtropical latitude water and
179 the Agulhas Current. Knowledge of the EMC retroflection variability will be key to un-
180 derstanding the variability of the Agulhas Current and the recirculation in the south-
181 west Indian Ocean. The disruptions of anticyclonic eddy pulses south of Madagascar due
182 to retroflection (Siedler et al., 2009) may induce sensitivity in the Agulhas Current Sys-
183 tem since mesoscale activities are the major source of Agulhas Current water (de Rui-
184 jter et al., 2004; Penven, Lutjeharms, & Florenchie, 2006). This may have an impact on
185 the magnitude of the Agulhas Current leakage (Figure 1j) (van Sebille et al., 2009), which
186 crucially regulates the connection between interocean exchanges in the Indian and the
187 Atlantic Oceans (Talley, 2013). On the other hand, the EMC is also connected with the
188 SICC (Menezes et al., 2016). The SICC is a shallow permanent current flowing from Mada-
189 gascar to western Australia between the latitudes of 20°S and 30°S. The SICC flows in

190 the opposite direction of the classical theories of wind-driven circulation (Menezes & Vianna,
191 2019) and is associated with a jet of salinity front and a subsurface thermal front in the
192 central Indian Ocean (Siedler et al., 2006; Palastanga et al., 2007), important for salt
193 and heat distribution in the Indian Ocean region. However, the link between the EMC
194 and the SICC is still not well defined to understand the advection of nutrient-rich from
195 the east coast of Madagascar favouring the formation of the Madagascar southeast phy-
196 toplankton bloom.

197 Very few studies have addressed the southern extension of the EMC, resulting in
198 the lack of an exact definition of the EMC retroreflection concept. Using multisensor satel-
199 lite and in situ cruise data, this study intends to describe the characteristics of the EMC
200 retroreflection and determine the associated dynamic processes and the local and regional
201 impacts.

202 **2 Data and Methods**

203 **2.1 In-situ data**

204 A compilation of vessel-mounted acoustic Doppler current profiler (VMADCP) mea-
205 surements was collected during five different research cruises operated around the EMC
206 retroreflection region. Explicit details of cruise data are given in Table 1. VMADCP data
207 operated by German research cruises were collected from the Data Publisher for Earth
208 and Environmental Science (PANGAEA: <https://www.pangaea.de/>). The two remain-
209 ing VMADCPs were obtained from the Institute Marine Research (IMR) database. Data
210 were already processed by their respective institution's holder. VMADCP data are used
211 to highlight the structure of the EMC at 25°S. Data are cropped only at the retroflec-
212 tion zone. Velocity components will be used to characterize the horizontal and vertical
213 structure of captured retroreflections.

214 A 2.5-year (10/2010 to 02/2013) time series of EMC volume transport (Ponsoni
215 et al., 2016) from a combination of several mounted acoustic Doppler current profilers
216 (ADCPs) and recording current metres (RCMs) deployed at 23°S are used to measure
217 the link between the daily volume transport of the EMC and the characteristics of its
218 associated retroreflection. To inspect the relationship between the EMC strength and its
219 retroreflection characteristics, we make use of a daily 2.5-year time series of the EMC vol-
220 ume transport estimated from in situ data. This time series spans from 10/2010 to 02/2013

221 and was provided by five vertical moorings deployed in a cross-shore transect at $\sim 23^\circ\text{S}$,
222 with the most inshore and offshore moorings placed at distances of approximately 6 and
223 110 km from the coast, respectively. To provide detailed information on the vertical ve-
224 locity and velocity shear structure at depths in which the EMC is stronger, each moor-
225 ing line was equipped with an upward-looking ADCP installed at a depth of approxi-
226 mately 500 m. Additionally, other ADCPs and

227 recording current metres (RCMs) were strategically deployed at different depths
228 depending on the mooring line. A sketch of the mooring lines and their respective in-
229 struments is shown in Ponsoni et al. (2016) (in their Fig. 2a). As described by these au-
230 thors, by time synchronizing the data sampled with all instruments, it was possible to
231 determine the alongshore velocities passing through the cross-shore transect from the seafloor
232 to the surface to provide an accurate estimation of the EMC volume transport. For a
233 complete description of the methodology used for the data processing and volume trans-
234 port computation, the reader is referred to Ponsoni et al. (2016) (in their Section 2).

235 We use quality-controlled surface drifter data from the Global Drifter Program (Lumpkin
236 & Pazos, 2007). The data spanned from February 1979 through June 2020. Data have
237 global coverage within more than 85% of the ocean surface (Maximenko et al., 2012).
238 The drifters have a battery life of up to 5 years, and the post-processed data yield ge-
239 olocations of the buoys every 6 h (Lumpkin et al., 2012). Drifters are advected with near-
240 surface flow (Niiler, 2001; Lumpkin et al., 2012). These can be used to study the direc-
241 tion and follow trajectories of ocean currents, such as retroflexion. All available surface
242 drift trajectories passing in the EMC region are collected from the Global Drifter Pro-
243 gramme database (Global Drifter; [https://www.aoml.noaa.gov/phod/gdp/interpolated/
244 data/subset.php](https://www.aoml.noaa.gov/phod/gdp/interpolated/data/subset.php)). This selects drifter trajectories targeting the fate of the EMC south-
245 ern extension, thus with a retroflexion or not.

246 2.2 Satellite Data

247 Altimetric sea surface height (SSH) data were collected from the Copernicus Ma-
248 rine and Environment Monitoring Service (CMEMS; <http://marine.copernicus.eu>).
249 The delayed-time dataset is a merged product from multiple altimeters (Ducet et al., 2000)
250 and is available on a 0.25° horizontal grid resolution as daily outputs from 1993 until the
251 present. The SSH product is the global ocean gridded L4 sea surface height and derived

252 variables reprocessed, collected from (Copernicus; <http://marine.copernicus.eu/services>
253 [-portfolio/access-to-products/?option=com_csw&view=details&product_id=SEALEVEL](http://marine.copernicus.eu/services-portfolio/access-to-products/?option=com_csw&view=details&product_id=SEALEVEL)
254 [_GLO_PHY_L4_REP_OBSERVATIONS_008_047](http://marine.copernicus.eu/services-portfolio/access-to-products/?option=com_csw&view=details&product_id=SEALEVEL_GLO_PHY_L4_REP_OBSERVATIONS_008_047)). Velocity field data are retrieved from the global
255 total surface and 15 m current (Copernicus-Globcurrent) from altimetric geostrophic cur-
256 rents and modelled Ekman current reprocessing (<http://marine.copernicus.eu/services>
257 [-portfolio/access-to-products/?option=com_csw&view=details&product_id=MULTIOBS](http://marine.copernicus.eu/services-portfolio/access-to-products/?option=com_csw&view=details&product_id=MULTIOBS)
258 [_GLO_PHY_REP_015_004](http://marine.copernicus.eu/services-portfolio/access-to-products/?option=com_csw&view=details&product_id=MULTIOBS_GLO_PHY_REP_015_004)). Data are used to derive the estimated geostrophic velocity of
259 EMC and to detect the retroflection spatial extent for the period 1993 to 2017.

260 The surface current products are obtained from the GlobCurrent project (Johannessen
261 et al. (2016); <http://www.globcurrent.org>). Based on multisatellite altimetry data
262 from 1993 to 2015, daily estimates of surface geostrophic currents are provided at a spa-
263 tial resolution of 25 km. Three-hourly Ekman currents (at the surface and 15 m depth)
264 are estimated from Argo floats, surface drifter and near-surface winds, and combined with
265 the velocity data. They are combined as monthly composites for this study. More de-
266 tails on how GlobCurrent data are produced and their limitations can be found in Rio
267 and Santoleri (2018), Feng et al. (2018), and Cancet et al. (2019).

268 The Optimum Interpolation Sea Surface Temperature (OISST) products version
269 2.1 are used to measure the surface signature of the coastal upwelling south of Mada-
270 gascar (Reynolds et al., 2007). SST products were obtained from the National Centers
271 for Environmental Information (NOAA; <https://www.ncdc.noaa.gov/oisst>). SST has
272 a spatial grid resolution of 0.25° and a monthly temporal resolution.

273 Monthly chlorophyll-a concentration data were obtained from the MODIS chlorophyll-
274 a level 3 (MODIS; <http://oceancolor.gsfc.nasa.gov/cgi/l3>) 4 km resolution grid,
275 covering the period of 2002 to 2017. Chlorophyll concentration is used to characterize
276 the response of the southeast Madagascar phytoplankton bloom to early retroflection.

277 **2.3 Retroflection tracking**

278 The EMC retroflection is identified from altimetry by selecting a specific SSH con-
279 tour as a streamline representative of the EMC path. The selected contour is chosen as
280 the mean sea level in the EMC southern extension region (42°E to 50°E and 22°S to 28°S),
281 over a bathymetry ranging from 200 m to 2000 m, and with current speeds higher than
282 35 cm s^{-1} . The westernmost contour position determines the EMC retroflection loca-

283 tion. This methodology is equivalent to the one applied to the Agulhas current by Backeberg
 284 et al. (2012), Loveday et al. (2014), and Renault et al. (2017).

285 **2.4 K-mean clustering**

286 The unsupervised K -mean clustering method is applied to define the spatial dis-
 287 tribution of the EMC retroflection turning points over time. K -means clustering is an
 288 unsupervised classification approach usually used to define undetected patterns in data
 289 (Hartigan & Wong, 1979). The classification method assigns samples, each data point,
 290 to belong to an identified k class. Classes are defined according to the density of par-
 291 titioned data. A point is determined to belong to a cluster based on a calculation of its
 292 Euclidian distance metric from a cluster centre called the barycentre (Ye et al., 2007; Singh
 293 et al., 2013). The barycentres are placed at a minimum distance possible to the optimal
 294 classified points. The assigned group is identified according to their minimum classic Eu-
 295 clidian distance metric of the detected EMC retroflection positioning expressed here as
 296 $Dist(x_i, y_i) = \sqrt{\sum_{i=1}^n (x_i - c_x)^2 + (y_i - c_y)^2}$. where $Dist$ is the Euclidean distance met-
 297 ric between barycentre c and n samples. (x_1, x_2, \dots, x_n) and (y_1, y_2, \dots, y_n) are samples
 298 coordinates. (c_x, c_y) is the barycentre spatial positioning (Singh et al., 2013; AbdAllah
 299 & Shimshoni, 2016).

300 Two instances of classification are performed to maximize the efficiency of the clas-
 301 sification applied to a large data dispersion (White et al., 2010). The first instance con-
 302 sists of separating the data into two main classes: the retroflection class and the no retroflec-
 303 tion class. The second instance afterwards focuses on classifying the retroflection class
 304 into two new classes. This approach is applied to obtain precision on the retroflection
 305 class distribution and the lowest standard deviation of the spatial distribution.

306 **2.5 Mesoscale eddy activity**

307 Altimetry gridded data are used to generate monthly vorticity and monthly eddy
 308 kinetic energy (EKE) for the period 1993 to 2017. Vorticity is performed to identify po-
 309 tential rotative circulation in the retroflection areas, expressed as follows: $\zeta = \frac{\partial v}{\partial x} -$
 310 $\frac{\partial u}{\partial y}$, where v and u are the meridional and zonal surface velocities (Ridderinkhof et al.,
 311 2013). The EKE is computed to quantitatively examine the signature of mesoscale eddy
 312 activities in the retroflection areas. EKE is calculated by using $\frac{1}{2}(u'^2 + v'^2)$ (Jia et al.,

2011), where u' and v' are the zonal and meridional geostrophic velocity anomalies, respectively.

The barotropic energy conversion rate quantifies the transfer of momentum between the mean flow and mesoscale eddy activities (Ma & Wang, 2014). In this study, the barotropic energy conversion rate is calculated to evaluate the energy exchanged between the impinging eddies arriving from the central Indian Ocean (de Ruijter et al., 2004; Quartly et al., 2006) and the EMC. The barotropic energy conversion rate is expressed as follows (R. Raj et al., 2016):

$$Br = -\overline{u'u'}\frac{\partial\bar{u}}{\partial x} - \overline{u'v'}\frac{\partial\bar{u}}{\partial y} - \overline{u'v'}\frac{\partial\bar{v}}{\partial x} - \overline{v'v'}\frac{\partial\bar{v}}{\partial y} \quad (1)$$

u' and v' are zonal and meridional geostrophic velocity anomalies, respectively. u and v are the surface geostrophic current velocities. The monthly gridded altimeter satellite product explained in section 2.2 was used to determine the barotropic energy conversion rate. The positive values of Br indicate a transfer of energy from the mean flow to the eddy field, while negative values imply energy transfer from the eddy field to the mean flow (Ma & Wang, 2014; R. Raj et al., 2016).

2.6 Eddy tracking algorithm

Automatic eddy-tracked data derived from multimission altimetry eddy trajectories are used to estimate eddy characteristics and trajectories in the retroreflection area. Mesoscale eddy locations and trajectories in the retroreflection area were obtained from the fourth release of an existing eddy global dataset (Chelton et al., 2011). It is an automated eddy algorithm that tracks eddies from daily sea surface heights (on a 0.25° Cartesian grid), derived from the delayed-time "two-sat merged" product of archiving, validation and interpretation of satellite oceanographic data (AVISO). The eddies are detected from a "growing method" (Schlax & Chelton, 2016), starting with identifying individual SSH extrema (negative for cyclones and positive for anticyclones) and locating all neighbouring pixels with SSH values lying above a sequence of thresholds. When a set of connected pixels satisfies a set of criteria used to define coherent and compact structures, an eddy is defined. The tracking of eddies is then performed by pairing eddy structures that are within allowable ranges of distance, radius and amplitude of the initial eddy at subsequent time steps. These global mesoscale eddy trajectory products (Delepouille

342 et al., 2018) are obtained directly from the AVISO website (<http://www.aviso.oceanobs>
 343 [.com/duacs/](http://www.aviso.oceanobs.com/duacs/)).

344 **2.7 Virtual particles simulation**

345 A Lagrangian experiment is applied to demonstrate the capacity of early retroflec-
 346 tion rerouting particles offshore east of Madagascar. Virtual particles were seeded in the
 347 core of the EMC, a one-degree grid poleward from the SEC bifurcation position ($\sim 18^\circ\text{S}$)
 348 (Chen et al., 2014), at the following coordinates of 50°E and 18°S . Particles were advected
 349 forward in time using daily altimetry-derived surface current and surface meridional and
 350 zonal velocity components from the gridded altimetry data (Liu et al., 2014).

351 **3 Results**

352 **3.1 Hydrographic observation of the EMC southern extension charac-** 353 **teristics**

354 Figure 2 illustrates a series of captured sea surface velocities and sections of merid-
 355 ional velocity recorded from VMADCP data. Sea surface height from gridded altime-
 356 try data at the same period of the recorded data are added to follow the pattern of cir-
 357 culation seen in the VMADCP. VMADCP data reveal the horizontal structure of the EMC,
 358 characterized by a narrow poleward jet, close to the shelf break around 25°S , with an av-
 359 eraged core velocity of 45 cm s^{-1} (Figure 2a-e). On the eastern side of the EMC 25°S ,
 360 an opposite flow is observed, $\sim 160\text{ km}$ from the coast, with an average velocity of 40
 361 cm s^{-1} (Figure 2a-e), consistent with Nauw et al. (2008).

362 All sections present opposite meridional velocities between the EMC and the re-
 363 turn flow (Figure 2a-e). However, while the EMC meridional velocity is consistently in-
 364 tense beyond a depth of $\sim 250\text{ m}$, the return flow starts to weaken below 100 m (Fig-
 365 ure 2f-j). Small differences in surface velocities and significant differences in meridional
 366 velocities at depth could be indicative of eddy-mean flow interactions when anticyclonic
 367 eddies shallower than the EMC approach the Madagascan coast near 24°S . Eddy-EMC
 368 interactions may induce a transfer of momentum towards the mean flow (Halo et al., 2014).
 369 Nauw et al. (2006) also reported an anticyclonic shear close to the core of EMC in the
 370 observed vertical transect from VMADCP at 25°S (see their Figure 5a).

371 Altimeter SSH is overlaid on top of VMADCP surface velocities. Good agreement
 372 is found between both datasets (Figure 1b-e). A high value of SSH (> 140 cm) delin-
 373 eates circular features indicative of anticyclonic eddies, a similar approach used in Ridderinkhof
 374 et al. (2013). VMADCP surface velocity captured anticlockwise rotative flow occurring
 375 at the edge of the high SSH approaching the continental shelf (Figure 2b-e). Several stud-
 376 ies (de Ruijter et al., 2004; Quartly et al., 2006; Anggoro et al., 2017; Ridderinkhof et
 377 al., 2013; TERNON et al., 2014) have used observations of sea level heights to identify ocean
 378 circulation patterns and eddy features. Sea level anomaly products are frequently used
 379 to characterize mesoscale eddy behaviours and characteristics; however, many studies
 380 have also applied SSH to identify and track the presence of mesoscale eddies (Ridderinkhof
 381 et al., 2013; Laxenaire et al., 2020). Thus, Figure 2b-e shows patterns of anticyclonic ed-
 382 dies drifting between 22°S and 24°S from the Indian Ocean to the Madagascar coastline,
 383 in agreement with Quartly et al. (2006) and Dilmahamod et al. (2018). The anticyclonic
 384 eddies appear to merge or disintegrate in the EMC around 25°S .

385 SSH maps, using the gridded altimetry product, shown in Figure 2b-e are reillus-
 386 trated in Figure 3a-d in a larger domain. The retroreflection tracking positioning explained
 387 in section 2.3 is applied to the enlarged SSH maps. Retroreflection positioning, indicated
 388 by blue stars, is identified during the same period of the collected VMADCP: Figure 3a
 389 and c detect retroreflections further downstream in the Agulhas Current region, which is
 390 indicative of no EMC retroreflection, while Figure 3b and Figure 3d show retroreflections
 391 in the southern extension of EMC. Interestingly, while Figure 3b reveals a retroreflection
 392 beyond the southern tip of Madagascar, Figure 3d shows the presence of a retroreflection
 393 prematurely formed along the southeast coast of the island. This retroreflection appears
 394 to start farther upstream, in the vicinity of 25°S , before progressing downstream.

395 **3.2 Three states of retroreflection extent**

396 Figure 4 depicts trajectories of available drifters passing inside the EMC core il-
 397 lustrated by the red rectangle from February 1979 to June 2018. Nineteen drifters fol-
 398 lowed an early retroreflection of the EMC (Figure 4a). Another 11 drifters follow the retroflec-
 399 tion around the southern tip of the island (Figure 4b). Finally, 18 drifters joined the Ag-
 400 ulhas Current, exhibiting no retroreflection (Figure 4c). On average, drifters take a few
 401 months to one year to travel from the EMC box to the east off 60°E during a premature
 402 retroreflection event at 25°S (Figure 4a). Some drifters, which return back to the Indian

403 Ocean further south, take approximately one year and a half to reach the offshore east
 404 of the island. In the no retroreflection case, drifters travel two to three years to delineate
 405 the subtropical early gyre in the Southwest Indian Ocean (Figure 4c). A list of all drifters
 406 and a statistical summary are presented in Table 2. Drifter trajectories basically reached
 407 opposite locations, where 37.5% of drifters joined the Agulhas Current, while 62.4% of
 408 the remaining drifters returned back to the Indian Ocean through retroreflection.

409 Monthly EMC retroreflection positions are detected from the gridded satellite altime-
 410 try over the 1993 to 2017 period. The retroreflection position is the westernmost of the
 411 selected SSH contour satisfying the conditions explained in section 2.3 to encompass the
 412 EMC flow. Figure 5a, b, and c show the mean position of the EMC retroreflection for each
 413 retroreflection mode (red stars). These are generated by averaging the satellite data (see
 414 contours and isoline of SSH) of the composite for each retroreflection type. Figure 5d high-
 415 lights the spatial distribution of the EMC retroreflection partitioned using the k -mean clus-
 416 tering method, assuming the existence of three classes. Each classified retroreflection po-
 417 sition is combined to build, according to retroreflection types, the mean position compos-
 418 ite mentioned in Figures 5a, b, and c. The three distinct cases of EMC retroreflection ob-
 419 tained are early retroreflection, canonical retroreflection, and no retroreflection. Both drifter
 420 trajectories (Figures 4a, b, and c) and satellite data (Figures 5a, b, and c) confirm the
 421 presence of three EMC retroreflection case scenarios. On monthly timescales during the
 422 period 1993 to 2017, an EMC retroreflection is identified over 47% of events (early retroreflec-
 423 tion: 13%; canonical retroreflection: 34%). The 53% remaining correspond to the case when
 424 the flow does not retroreflect and propagates straight into the Agulhas system. This is in
 425 line with the findings of Siedler et al. (2009) with the addition of the early retroreflection
 426 case as a new state of the EMC.

427 The EMC early retroreflection is the upstream eastward drift of EMC from the east
 428 coast of Madagascar. The highest longitudinal probability of the early retroreflection po-
 429 sition is at $47.6^{\circ}\text{E}\pm 0.41$, while it is at $43.8^{\circ}\text{E}\pm 1.8$ for the canonical retroreflection (Figure
 430 5b). Early retroreflection latitudinal average positioning is 25.65°S (Figure 5f). Table 3
 431 summarizes the occurrence and position of the retroreflection types.

3.3 Description of Early Retroreflection events

To address the drivers of early retroreflection events, we use an integrated EMC volume transport time series collected from ADCPs and RCMs combined data (Ponsoni et al., 2016). In addition, EMC geostrophic velocity, provided by the gridded altimetry data, is retrieved from the nearest location of the moored ADCPs. On daily time scales, a significant linear relationship, a correlation coefficient factor of 0.61 at a 95% confidence level, is found between the two time series, which are the southward volume transport and the surface geostrophic velocity of the EMC (Figure 6a, b).

The daily EMC retroreflection position is tracked over the period coinciding with the ADCP deployment from 01/10/2010 to 01/02/2013. The results reveal that the occurrences of early retroreflections coincide with intense southward EMC volume transport (Figure 6a,c). During the time period of 11/10/2010 to 01/04/2013, early retroreflection positions persisted for an average of 15 days, depending on the number of occurrences. An early retroreflection is also found to persist over two months (12/2010 to 01/2011) when the southward EMC volume transport peaked at 45 Sverdrup (Sv) ($1 Sv = 10^6 m^3 s^{-1}$), while it did not occur for four consecutive months (03/2012 to 06/2012) when the transport is $\sim 18 Sv$, which is the average transport of the EMC at this latitude (Ponsoni et al., 2016; Ramanantsoa, 2018b). In summary, the likelihood of early retroreflection increases with the volume of EMC transport and drops when the volume transport is low.

Time periods with intense volume transport (above one standard deviation) are used to construct composite means of SSH and ocean colour. Figure 7a and 7b present characteristics of an early retroreflection at 24.5°S. This link between high volume transports and earlier retroreflections is consistent with the results of previous theoretical work in the Agulhas system (Ou & De Ruijter, 1986), suggesting that the interaction between coastline curvature and high transport of the Agulhas Current tends to favour early retroreflection. This finding is reinforced by Arruda et al. (2014). These authors have shown that variations in the Rossby number of deformation seem to induce inertial and momentum imbalances of the Agulhas Current and, as consequence, generate an upstream retroreflection (the so-called Agulhas Current early retroreflection). Figure 7a shows that the EMC early retroreflection appears to originate from 24.5°S (black star) and that the EMC flow seems to drift eastward following a zonal band at $\sim 25.5^\circ S$. A high value of SSH is observed in that position, indicative of an anticyclonic rotation, which seems to be respon-

464 sible for the early eastward drift at this latitude. This is also seen in Figure 7c, which
465 depicts intense positive vorticity over a wide range, indicative of anticyclonic circulation
466 along the east coast but not necessarily anticyclonic eddies. However, mesoscale anti-
467 cyclonic eddies are known to drift from the central Indian Ocean and propagate into the
468 EMC (de Ruijter et al., 2004; Dilmahamod et al., 2018). Accordingly, the wide range
469 of positive vorticity could be the signature of the anticyclonic presence. Hence, the ar-
470 rival of anticyclonic eddies increases the EMC strength, which is in line with (Ponsoni
471 et al., 2016) and induces an abrupt detachment of the flow from the coast. The intense
472 volume transport of the EMC (Figure 6a) together with the contribution of mesoscale
473 eddies promotes early retroreflection occurrences (Figure 7a). In addition, the early de-
474 tachment of the EMC also presents a signature in chlorophyll-a extending from the up-
475 welling south of Madagascar (Ramanantsoa et al., 2018a) to more than 2° longitude off-
476 shore towards the east (Figure 7b). This shows that early retroreflection can trigger phy-
477 toplankton bloom patches, usually occurring in this region, as suggested in Dilmahamod
478 et al. (2019).

479 Two synoptic developments of the EMC early retroreflection from the onset to the
480 full formation are illustrated in Figures 8 and 9. These figures intend to demonstrate a
481 synoptic preformation of early retroreflection associated with an anticyclonic eddy using
482 the automatic eddy-tracked data explained in the data section, propagating from the In-
483 dian Ocean towards the south of Madagascar. Propagations of high sea level agree well
484 with the westward movement of anticyclonic eddies reaching the edge of the EMC. An
485 anticyclonic eddy seems to trigger the eastward veering of the EMC. It enhances the flow
486 to consequently form an early retroreflection. Although it is difficult to provide a detailed
487 explanation of how the anticyclonic eddy detaches the core of the EMC to drift eastward,
488 Figure 8 illustrates only the altimetric observation of the early retroreflection formation
489 from a synoptic development perspective. Figure 9 also shows a similar process, while
490 it shows the eventual shift from a canonical retroreflection case to an early retroreflection
491 case. This confirms the progressive arrival of high sea surface heights reaching 160 cm
492 (in line with Figure 2), overlapping with anticyclonic eddy tracking. It also reinforces
493 the link between the preformation of an early retroreflection and the association with an-
494 ticyclonic eddies. Virtual particles were released in the EMC core to coincide with the
495 synoptic early retroreflection period. This emphasizes the argument that the early retroflec-

496 tion triggers a premature eastward transport of water and is responsible for the advect-
 497 ion of EMC water parcels and perhaps nutrients towards the centre of the Indian Ocean.

498 **3.4 Dynamical processes**

499 Figures 10 and 11 demonstrate the dual roles of the EMC strength and the mesoscale
 500 activities defining the type of retroflection. Figure 10 presents the occurrences of retroflec-
 501 tion cases, the EMC surface geostrophic velocity anomalies, and the surface eddy kinetic
 502 energy for the period 1993 to 2017. Occurrences of retroflection cases are highlighted by
 503 red-shaded bands for the early retroflection, while blue-shaded bands depict canonical
 504 retroflection over the period of the study. Moreover, blank spaces in between account
 505 for the period of no retroflection events. Time series: (1) Grey time series is the monthly
 506 anomaly of the EMC surface current speed, generated from the gridded satellite altime-
 507 try, already used in Figure 6b, and (2) green and blue time series are the eddy kinetic
 508 energy (EKE) extracted from early- and canonical retroflection areas, respectively. These
 509 areas are illustrated by rectangles in Figure 11a and b. The computation of the EKE
 510 is explained in section 2.5.

511 Figure 11a, b, and c show the EKE mean composite of each retroflection type, sim-
 512 ilarly performed as in Figure 5a, b, and c. Figure 11d, e, and f show the results of the
 513 mean composite characterized by both EMC current strength and EKE intensity vari-
 514 ations highlighted in Figure 10. Figure 11d is the mean composite of SSH associated with
 515 anomalously high EMC surface speeds (above one standard deviation), extracted near
 516 the ADCP mooring location, and anomalously high EKE extracted from the early retroflec-
 517 tion area (above one standard deviation in the green box in Figure 11a). The mean com-
 518 posite of each retroflection type is then assessed. In agreement with the previous sec-
 519 tion, it corresponds to an early retroflection. Positive abnormally high EMC speeds tend
 520 to promote early retroflection. Moreover, anticyclonic eddies from the Indian Ocean also
 521 induce an enhancement in EMC speeds and promote an early eastward drift of the EMC
 522 southern extension in the vicinity of $\sim 25^\circ\text{S}$. The synoptic development illustrated in Fig-
 523 ure 8 has confirmed the involvement of anticyclonic eddies triggering early retroflection,
 524 and the retroflection mode can be shifted from a canonical retroflection type to an early
 525 retroflection highlighted in Figure 9. This also highlights how the presence of a high EKE
 526 in Figure 11a may be associated with the arrival of anticyclonic eddies as a cause of the
 527 early retroflection event but not its consequence.

528 A negative linear relationship with a correlation coefficient equal to 0.3, significant
529 at 95% confidence, is found between the EMC speed and EKE in Figure 10 extracted
530 from the canonical retroflection area illustrated as a blue box in Figure 11b. Figure 11e
531 depicts the composite obtained for weaker EMC speeds (below one standard deviation)
532 but with a more intense EKE (above one standard deviation) in Figure 11b. The retroflec-
533 tion type of the mean composite resulted in canonical retroflection. This reveals that the
534 canonical retroflection pattern is associated with a decrease in EMC surface speeds and
535 the generation of eddy dipoles after EMC separation on the leeward of the southern tip
536 of Madagascar (Ridderinkhof et al., 2013). Based on de Ruijter et al. (2004) and Ridderinkhof
537 et al. (2013), eddy dipoles are typical patterns of the EMC southern extension, explain-
538 ing the higher EKE seen when EMC is in a canonical retroflection mode.

539 The third pattern in Figure 11f is obtained from a mean composite of SSH asso-
540 ciated with decreased EKE (below one standard deviation) in both early and canonical
541 areas (blue and green boxes in Figures 11a and 11b). This corresponds to a no retroflec-
542 tion case. In this case, a straight flow towards the African continent is associated with
543 a minimum in eddy activity in the early and canonical retroflection areas.

544 Figure 12 shows the capacity of retroflection areas to receive drifted anticyclonic
545 eddies arriving from the central Indian Ocean. It shows trajectories of mesoscale anti-
546 cyclonic eddies from the east into the retroflection areas. Figure 12a shows the arrival
547 of anticyclonic eddies ending into the early retroflection areas, while Figure 12b depicts
548 anticyclonic eddy trajectories ending life in canonical retroflection areas. Their presence
549 is consistent with the indicated locations for retroflections (green and blue stars in Fig-
550 ure 10d and e), which show the presence of remarkable EKE at each attributed retroflec-
551 tion location (blue and green boxes in Figures 10a and 10b). This is in line with the find-
552 ings highlighted in Figure 8 and 9 regarding eddy activity involvement triggering retroflec-
553 tions. Hence, the presence of EMC retroflection is often associated with mesoscale ed-
554 dies occurring in both the early retroflection and canonical retroflection areas. The eddy
555 tracking method is limited to show the interaction between eddies and the mean flow.
556 Although eddy tracking shows the presence and path of eddies, it is limited to reveal-
557 ing their interactions with the EMC if anticyclonic eddies are disintegrated or continue
558 their paths after triggering retroflection. This is consequently not an appropriate approach
559 to demonstrate eddy-mean flow interactions in this case. Laxenaire et al. (2020) explained
560 the complex fate of eddies when satellite altimetres could no longer track mesoscale ed-

561 dies during eddy tracking processes. Mesoscale eddies can take different forms after no
 562 longer being monitored by tracking eddy methods (Laxenaire et al., 2020). Hence, the
 563 eddy trajectories, through the eddy-tracking method, are insufficient to understand and
 564 explain the contribution of mesoscale eddy triggering retroflection.

565 To enlighten the dynamical interaction between eddy-mean flow leading instabil-
 566 ities of the EMC, the surface barotropic energy conversion rate is calculated to estimate
 567 the transfer of momentum between the mesoscale eddy and the mean flow (Figure 13).
 568 Since anticyclonic eddies contribute to the formation of retroflection, eddy activities in
 569 the retroflection areas will be mostly attributed to anticyclonic eddy dynamics. Figure
 570 13 illustrates the surface barotropic energy conversion rate during the whole period of
 571 early and canonical retroflection combined (Figure 13a) and during the period of no retroflec-
 572 tion (Figure 13b). Clear differences in transferred energy are found southeast of Mada-
 573 gascar during these periods. The Mozambique channel side is also included intention-
 574 ally in Figure 13 to show that other regions do not differ more in terms of energy dur-
 575 ing the period of retroflections. The dipole of transferred energy is located southeast of
 576 the island ($\sim 25^\circ\text{S}$), in line with Halo et al. (2014) (see Figure 13a-d). A negative value
 577 implies the transfer of energy from the mesoscale eddies to the mean flow, and a pos-
 578 itive value implies the opposite. Figure 13a reveals a strong flow of kinetic energy on the
 579 order of $2.3 \cdot 10^{-6} \text{ m}^2 \text{ s}^{-3}$ (negative value), is transferred from the eddy field to the EMC
 580 in the vicinity of 25°S . Figure 13b shows less transfer of momentum during the no retroflec-
 581 tion event, indicated by only $0.8 \cdot 10^{-6} \text{ m}^2 \text{ s}^{-3}$ (negative value). This reveals the inter-
 582 action of anticyclonic eddies with the EMC in the early retroflection area. On the other
 583 hand, a flow of intense energy exceeding $2.3 \cdot 10^{-6} \text{ m}^2 \text{ s}^{-3}$ (positive value), is observed
 584 in the southern extension of the EMC (Figure 13a). This is due to the transfer of en-
 585 ergy from the mean flow to the eddy. This reveals the capacity of the EMC southern ex-
 586 tension propelling eddies, documented in de Ruijter et al. (2004), Ridderinkhof et al. (2013),
 587 and Halo et al. (2014), which trigger the condition towards formation of canonical retroflec-
 588 tion at the southern tip explained in the previous paragraph. The case of less energy mo-
 589 mentum in Figure 13b is characterized by less eddy activity and a stable EMC and, hence,
 590 no retroflection. The findings corroborate to the results in Figure 11, showing that high
 591 EKE in the retroflection areas promotes retroflection, while less EKE in both locations
 592 implies no retroflection. Hence, it is now demonstrated that high EKE located at the

593 retroflection areas are indicative of eddy activities associated with the EMC to trigger
 594 retroflections.

595 In summary, the EMC early retroflection is linked with EMC strength. Anticyclonic
 596 eddies drifting from the central Indian Ocean to the east Madagascar coast favour early
 597 retroflection formation, anticyclonic eddies near the southern tip of Madagascar promote
 598 the generation of canonical retroflection, and no retroflection appears to be associated
 599 with a lower eddy kinetic energy (EKE), together with EMC strength modulation.

600 **3.5 Local and regional impact of the early retroflection**

601 The retroflection structure allows an estimated lagged response with the south Mada-
 602 gascar coastal upwelling cell strength (Ramanantsoa et al., 2018a)(Figure 14a). During
 603 an early retroflection, coastal upwelling became instantaneously weak (for one month),
 604 i.e., the upwelling cell surface temperature anomaly becomes warm, while EMC early retroflec-
 605 tion occurs. The average composite of the SST anomaly during the period of the early
 606 retroflection event shows an abnormally high temperature in the upwelling cell (Figure
 607 14b), while the period composite during the EMC canonical and no retroflection com-
 608 bined seems to be favourable for upwelling occurrences (Figure 14c). This behaviour is
 609 probably due to the interruption of the topographically induced upwelling mechanical
 610 process (Ramanantsoa, 2018b) that occurs during an early retroflection. The disruptions
 611 of the southward EMC flow, due to premature eastward veering causing the early de-
 612 tachment of the EMC from the coast, may inhibit the mechanism generating the upwelling
 613 strength of southeast Madagascar, so-called Core 1 (Ramanantsoa, 2018b), which is the
 614 bottom Ekman transport inducing upwelling over the topography and reinforced by favourable
 615 winds at inter-annually time scale (Ramanantsoa et al., 2018a).

616 A spatial coherent structure is found between composites of early retroflection cir-
 617 culation patterns and surface chlorophyll-a concentration during the same period (Fig-
 618 ure 7b). Moreover, Figure 15 reveals that the prevalence of the austral summer South-
 619 East Madagascar bloom as described by Dilmahamod et al. (2019) could be mainly as-
 620 sociated with an EMC early retroflection. Although this bloom generation is associated
 621 with multiple processes (Dilmahamod et al., 2019), the early retroflection could be a con-
 622 tributor to the summer bloom occurrence. In addition, the composite of surface currents
 623 built from early retroflection periods (Figure 15a) reveals that the EMC early retroflec-

624 tion structure could act as a contributor to SICC formation (Menezes et al., 2016). This
625 suggests that the transport of nutrient-rich water through the SICC from the east coast
626 could induce a visible offshore chlorophyll-a concentration patch (Figures 7b and 15b).
627 Moreover, virtual particle simulations during the synoptic development of early retroflec-
628 tion in Figures 8 and 9 reinforce the concept of offshore nutrient advection from the east
629 coast of Madagascar drifting towards the SICC. This finding agrees with Srokosz et al.
630 (2015) and Dilmahamod et al. (2019), who associated early retroflexion as a factor trig-
631 gering the prominence of phytoplankton blooms.

632 Hence, the occurrence of EMC Early Retroflexion has a contrasting effect: While
633 it perturbs the functioning of coastal upwelling south of Madagascar, it also tends to favour
634 the South-East Madagascar bloom. Both are important for biology and fisheries.

635 The disruptions of anticyclonic eddy pulses due to early retroflexion and canon-
636 ical retroflexion should be assessed if they induce sensitivity in the Agulhas Current Sys-
637 tem activities since mesoscale structures originating south of Madagascar are a major
638 source of Agulhas Current water (de Ruijter et al., 2004; Penven, Lutjeharms, & Flo-
639 renchie, 2006). A separate study should investigate the cascade effect of EMC retroflec-
640 tion on Agulhas Current retroflexion positioning if the Agulhas Current System remains
641 stable due to this disruption of energy transferred through eddies from EMC.

642 **4 Discussion and Conclusions**

643 Using a suite of cruise data measurements, in situ data, and satellite observations,
644 this study reveals the spatial extent of the EMC retroflexion. Three distinct types of
645 states are identified: early retroflexion, canonical retroflexion, and no retroflexion. The
646 classic retroflexion south of Madagascar, beyond the southern tip, is here defined as a
647 canonical retroflexion. The new state, the EMC early retroflexion, corresponds to the
648 current turning back offshore from the east coast of the island. A retroflexion position
649 detected close to the African coastline until further downstream in the Agulhas Current
650 System is described as no retroflexion. From 1993 to 2017, retroflexions occurred 47%
651 of the time, 13% of which were attributed to the early retroflexion. These findings cor-
652 roborate the results highlighted by Siedler et al. (2009), who revealed that almost 50%
653 of the EMC water feeds the Agulhas Current System, while $\sim 40\%$ contributes to SICC
654 formation.

655 By linking EMC strength and the mesoscale variability occurring in the retroflec-
656 tion areas, our study also shows how retroflexion can be formed. The retroflexion po-
657 sition is EMC strength dependent, i.e., anomalous EMC speed favour retroflexion, with
658 a significant eddy activity contribution. Synoptic development of early retroflexion demon-
659 strated the progressive formation of the premature eastward drift of the EMC core at
660 25°S after interacting with an anticyclonic eddy (Figures 8 and 9). The availability of long-
661 term observations of the EMC strength allowed us to conclude that the variability of EMC
662 volume transport (column water) varies with the occurrence numbers of early retroflec-
663 tion (Figure 6). The surface signature of this early retroflexion was subsequently ob-
664 served and confirmed by multisensor satellite products, altimeters and ocean colours (Fig-
665 ure 7). Hence, an intense current can promote early retroflexion occurrences in agree-
666 ment with processes described in Ou and De Ruijter (1986) during investigation of the
667 Agulhas Current retroflexion mode, as a western boundary current having similar char-
668 acteristics as the EMC.

669 The retroflexion type is defined by the variation in the EKE in the retroflexion
670 areas, early retroflexion and canonical retroflexion areas and is associated with EMC
671 strength modulation. Anomalously high EKE in these areas was demonstrated to trig-
672 ger the formation of retroflexion. Weaker EKEs in both the early retroflexion (east)
673 and canonical retroflexion areas (west) promote the no retroflexion case with a contin-
674 uous flow propagating from the EMC southern extension straight towards the Agulhas
675 Current without interruption (Figure 11). The findings respond to the question of how
676 the mesoscale eddy interacts with the EMC. Transfer of a strong EKE from the mesoscale
677 eddy field to the EMC is found during the retroflexion periods, while less transfer of mo-
678 mentum is implied during the no retroflexion period (Figure 12). Similar events of eddy-
679 current interactions have been described upstream of the Agulhas Current, where en-
680 trainment of anticyclonic eddies increases the current velocity and shifts the Agulhas Cur-
681 rent offshore (Braby et al., 2016). Additionally, the positive transfer of momentum (Fig-
682 ure 13a), from the mean flow to the eddy field, favours the presence of an anticyclonic
683 standing eddy at the southern tip of Madagascar propelled by the EMC before the for-
684 mation of eddy dipoles (de Ruijter et al., 2004; Ridderinkhof et al., 2013), which pro-
685 motes the canonical retroflexion case.

686 The irregular arrival of Rossby waves and impinged eddies, originating from the
687 Indian Ocean and congregating at 25°S (Schouten et al., 2002, 2003; de Ruijter et al.,

688 2004; Quartly et al., 2006; Halo et al., 2014), induced difficulties in clearly identifying
689 the original location of the EMC retroflection and the source of the SICC from VMADCP
690 observations (Figure 2). The combination of altimetry with in situ data reveals that an-
691 ticyclonic eddies passing through 25°S are associated with retroflection in addition to the
692 contribution of the EMC core strength. Since it was difficult to interpret the early retroflec-
693 tion as a retroflection in previous literature (J. Lutjeharms, 1988; Quartly & Srokosz,
694 2002), this study has devoted significant effort to showing the evidence, as well as to de-
695 scribing the dynamic processes and the impact of the early EMC eastward veering from
696 the coast at 25°S.

697 Identification of the EMC retroflection patterns leads to an understanding of their
698 influence on the southeastern Madagascar Bloom, coastal upwelling, and connection with
699 the SICC. Early retroflection has several effects on local ecosystems. It favours a pre-
700 vailing southeast phytoplankton bloom (Figure 14) but disrupts the prominence of coastal
701 upwelling, as seen in Figure 13a and b. According to Backeberg et al. (2012) (see their
702 Figure 4), mesoscale variability of the southwest Indian Ocean, including south of Mada-
703 gascar, has intensified due to the enhancement of trade winds over the tropical region.
704 This may increase EMC early retroflection in numbers due to the increase in mesoscale
705 eddy activity, and consequently, it may induce more southeastern Madagascar Bloom
706 but weaken coastal upwelling.

707 More in situ datasets, such as long-term observations and ARGO data, are required
708 for a better understanding of the physical mechanisms associated with western bound-
709 ary currents interacting with mesoscale eddies (anticyclonic and/or cyclonic). Moreover,
710 the effect of the EMC retroflection mode on the Agulhas Current and the Indian Ocean
711 gyre should be assessed in a separate study.

712 **Acknowledgments**

713 The authors want to thank the NRF SARCHi chair on Ocean Atmosphere Modeling and
714 the GdRI-Sud CROCO project for funding. The volume transport data were sampled
715 within the context of the INATEX program funded by Netherlands Organization for Sci-
716 entific Research (NWO), section Earth and Life Sciences (ALW), through its ZKO Grant
717 839.08.431. Datasets are available through the ZKO data portal (<http://data.zkonet.nl/>).
718 We thank Prof Martin Visbeck (GEOMAR) and Dr Raymond Roman (UCT) for pro-
719 viding some cruise datasets utilized in this study. Ocean dynamic topography data were

720 obtained from the Copernicus Marine Environment Monitoring Service (CMEMS) ([http://](http://marine.copernicus.eu/)
721 marine.copernicus.eu/). The global drifter data used in this study were collected from
722 the National Oceanic and Atmospheric Administration (NOAA), Physical Oceanogra-
723 phy Division (PhOD), and Global Drifter Program ([https://www.aoml.noaa.gov/phod/](https://www.aoml.noaa.gov/phod/gdp/)
724 [gdp/](https://www.aoml.noaa.gov/phod/gdp/)). The altimeter Mesoscale Eddy Trajectory Atlas products were produced by SSALTO/DUACS
725 and distributed by AVISO+ (<https://www.aviso.altimetry.fr/>) with support from CNES,
726 in collaboration with Oregon State University with support from NASA.

Table 1. Description of Vessel Mounted Acoustic Doppler Current Profiler (VMADCP) datasets used in the study with their associated periods, vessels and research cruises. The state of the availability of the VMADCP data on Figure 2c-e are in the process of being published by their respective institution holder.

VMADCP	Code	Vessel	Cruise name	Date	Doi
Figure 2a	199	RSS Discovery Survey	GEOMAR 1987	30-01-1987/21-02-1987	10.1594/PANGAEA.3196
Figure 2b	180	R.V. Knorr	GEOMAR 1995	11-06-1995/11-07-1995	10.1594/PANGAEA.3195
Figure 2c	300	R.V. Fridtjof Nansen	ASCLME 2008	01-09-2008/07-09-2008	-
Figure 2d	-	R.V. Meteor	M100-2	-10-2013/21-10-2013	-
Figure 2e	-	R.V. Fridtjof Nansen	Nansen 2018	28-10-2018/02-11-2018	-

Table 2. Summary of available global drifters showing three types of EMC retroflection. Table summarizes the drifters for each retroflection type, the period of traveling from the EMC to the central Indian Ocean, and the identity number of drifters.

	EMC Early Retroflection	EMC Canonical retroflection	EMC No retroflection
Percentage	39.5 %	22.9 %	37.5 %
Period	few months to 1 year	~ 1.5 year	2 to 3 years
Drifter N ^o	20333, 34157, 37631, 41243 41337, 41339, 42539 70963, 71090, 81834 88664, 90502, 109538 109539, 133655, 9421901 9730550, 63040060, 6482637	25020, 26219, 83341, 114826 2134150, 9729754, 9730550 61479400, 63043010, 63897000 63941920	43580, 44296, 54395, 63875 70942, 70957, 70969 70970, 81849, 83446 115991, 126948, 127314 127353, 2134164, 9619819 60609830, 60750130

Table 3. Statistical summary of retroflection. Lon. is longitudinal, while Lat. is latitudinal direction. Skewness measures dispersion of the variation to test if it is distributed more to the left (negative) or to the right (positive) of the average.

	Early Retroflection	Canonical Retroflection	No retroflection
Occurrences	13 %	34 %	53 %
Lon. mean position	$47.6^{\circ} \pm 0.41$	$43.8^{\circ} \pm 1.8$	$19.1^{\circ} \pm 5.37$
Lat. mean position	$25.6^{\circ} \pm 1.2$	$28.1^{\circ} \pm 0.4$	$40.1^{\circ} \pm 2.12$
Skewness	2.57 (Lat. position)	-1.29 (Lon. position)	3.74 (Lon. position)

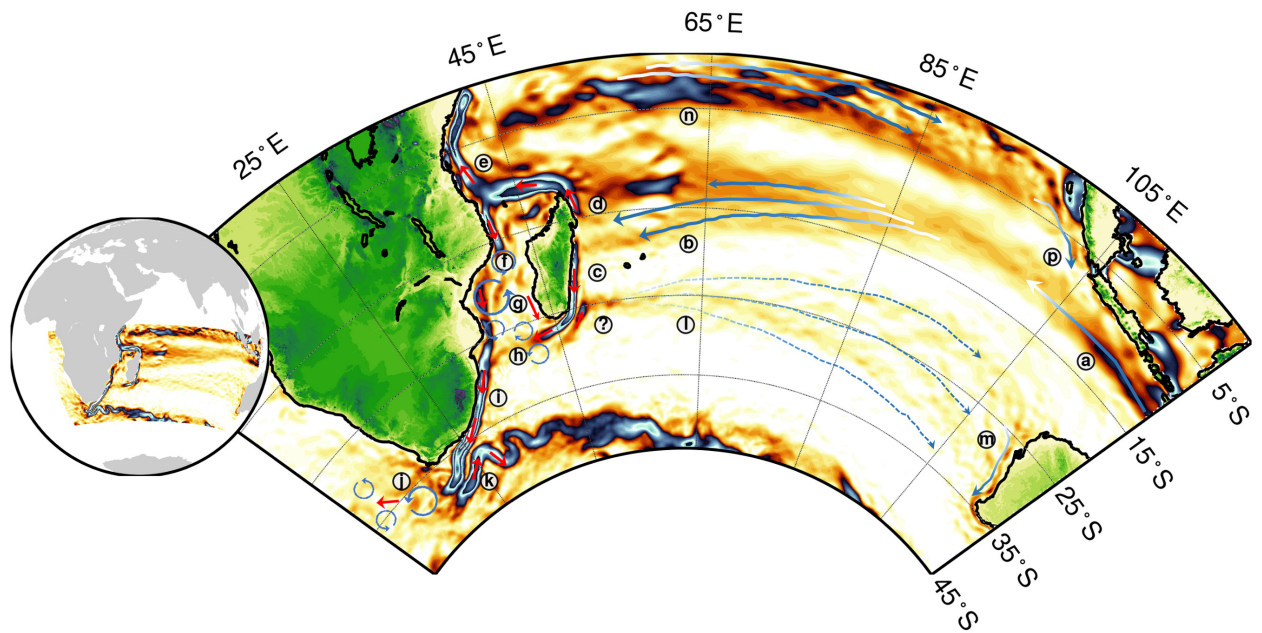


Figure 1. Schematic of the general ocean circulation in the South Indian Ocean. Schematic is built based on Wyrтки (1973); J. R. Lutjeharms (2006); Schott et al. (2009). Map shows South Indian Ocean currents features. The map is unitless and used for schematic illustration purposes only. Red arrows highlight coastal, western boundary currents, and their extensions. Plain blue arrows depict main offshore circulations. Dotted blue arrows illustrate nonpermanent offshore circulation.

a-Indonesian Throughflow (IT) (Sprintall et al., 2009), b- South Equatorial Current (SEC) (Chen et al., 2014), c- East Madagascar Current (EMC) (Ponsoni et al., 2016), d- North Madagascar Current (NMC) (Ponsoni, Aguiar-Gonzalez, et al., 2015), e- East African Coastal Current (EACC) (J. C. Swallow et al., 1991), f- Mozambique Channel anticyclonic eddies (Halo et al., 2014), g- Southwest Madagascar Coastal Current (SMACC) (J. D. Ramanantsoa et al., 2018), h- Dipole of eddies South of Madagascar (Ridderinkhof et al., 2013), i- Agulhas Current (AC) (J. R. Lutjeharms, 2006), j- Agulhas Rings (Olson & Evans, 1986), k- Agulhas Return Current (ARC) (J. Lutjeharms & Van Ballegooyen, 1988), l- South Indian Counter Current (SICC) (Menezes et al., 2016). m- Leeuwin Current (LC) (Feng et al., 2009), n- South Equatorial Counter Current (SECC) (Gordon et al., 1997), n- South Java Current (SJC) (Sprintall et al., 1999). The question mark located southeast of Madagascar indicates the unclear circulation connecting the EMC (c) and the SICC (l) replicated from Menezes et al. (2014).

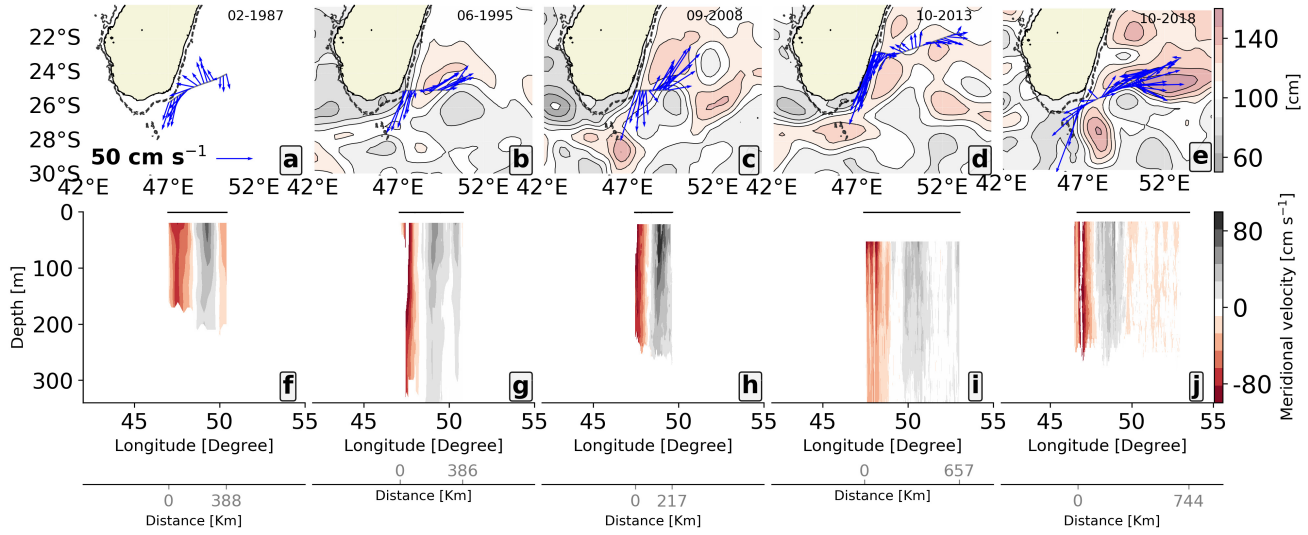


Figure 2. Hydrographic tracking of the EMC retroreflection at $\sim 25^{\circ}\text{S}$. Panels (a) to (e) are transects showing the horizontal structure of the current. Arrows represent directions and intensities of the near surface flow (~ 20 m). Grey lines, in which arrows originate, indicate the selected vessel trajectories. Overlapping maps show weekly SSH according to each VMADCP measurement period (bottom). Note that satellite altimetry data were not available during the 1987 cruise for the first panel (a). Black horizontal lines at 0 m present the measured distance scale of each transect. Panels (f) to (j) illustrate the vertical structure of the EMC southern extension measured at the same location from the VMADCP. The current vectors along each transect are projected onto the longitude axis, and their distances from the coast are measured from the closest coastline location.

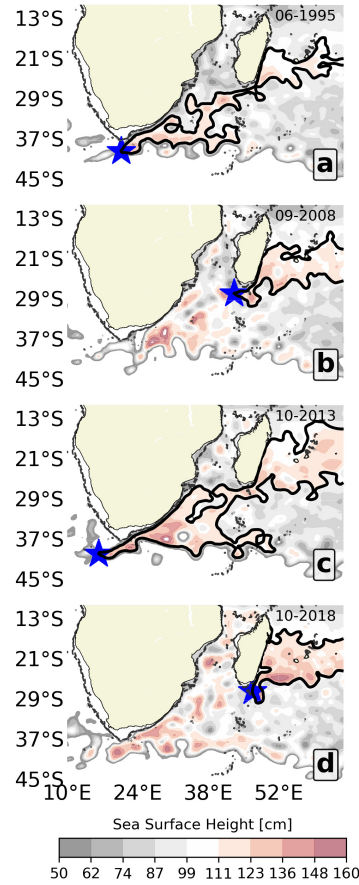


Figure 3. Altimeter satellite-based EMC retroreflection tracking. Panels (a) to (d) illustrate the EMC retroreflection position detection. Black lines are the detected SSH contours performed to track the EMC extension. Blue stars highlight the westernmost point of the contour, considered the EMC retroreflection position. Maps are the enlarged views of SSH maps seen Figure 2 (b) to (e).

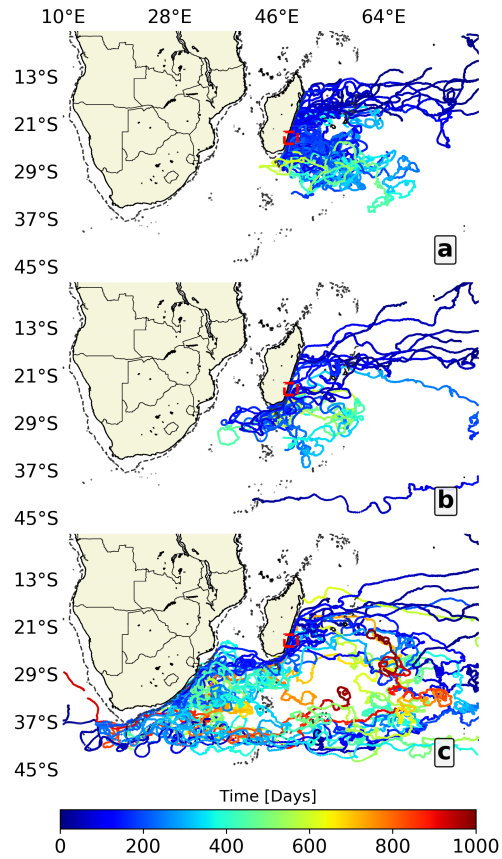


Figure 4. EMC retroflection spatial extent based on the global surface drifter dataset. Panels (a), (b) and (c) present trajectories and time durations of surface drifter floats depicting the three cases of EMC retroflection. (a) Selected surface drifters that follow the EMC early retroflection case. (b) Drifters that depict the EMC canonical retroflection. (c) Combined drifters that represent the EMC no retroflection case.

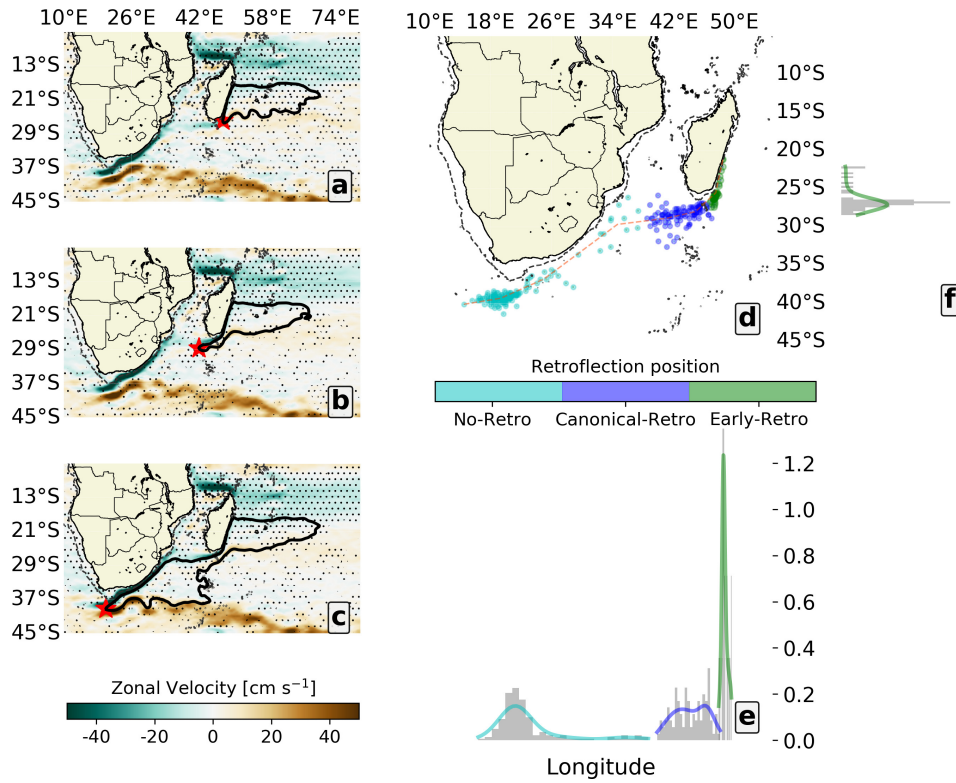


Figure 5. EMC retroflection spatial extent based on satellite altimetres. Panels (a), (b) and (c) display composites of detected EMC retroflection positions using the SSH from satellite altimetry. The black contour represents the EMC and its retroflection. Red stars highlight the westernmost point of the selected SSH contour, considered as the EMC retroflection position. The maps in the background represent composites of zonal velocity corresponding to each retroflection case. Hatched black dots indicate a 95% confidence level according to a two-tailed Student's *t*-test. (d) presents the spatial classification of the EMC retroflection position from the unsupervised *k*-mean clustering. The dotted red line delineates the most likely location of EMC retroflection positions. Each classified EMC retroflection case is used to build the composites of panels (a), (b) and (c). (e) displays the longitudinal distributions of the three EMC retroflection cases. (f) displays the latitudinal distribution for the early retroflection case.

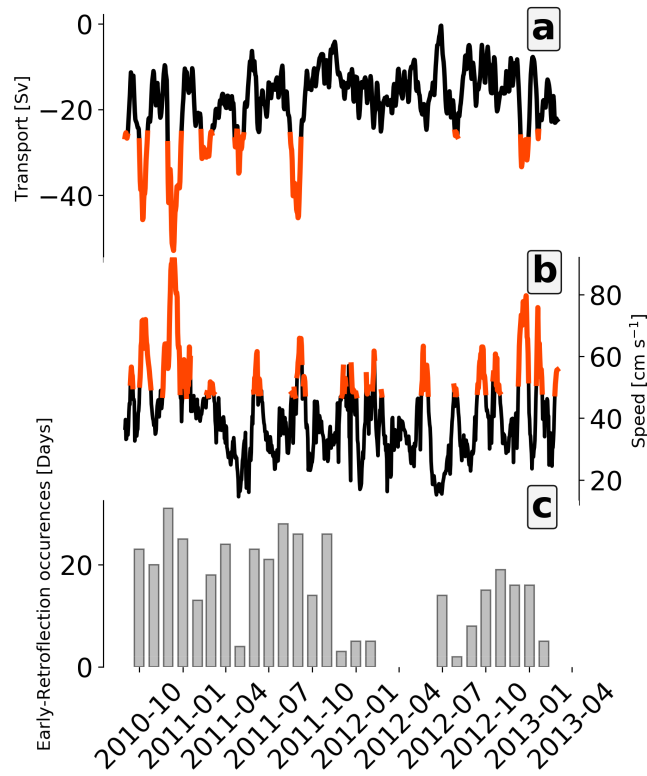


Figure 6. Evidence of the EMC early retroflection. (a) Time series of EMC northward volume transport from ADCP (Ponsoni et al., 2016). (b) Time series of the surface geostrophic currents from the satellite altimetry data at the same location ($\sim 23^{\circ}\text{S}$). EMC current speeds and volume transports higher than the standard deviation are highlighted in red. (c) Monthly EMC early retroflection occurrences computed from the detection algorithm.

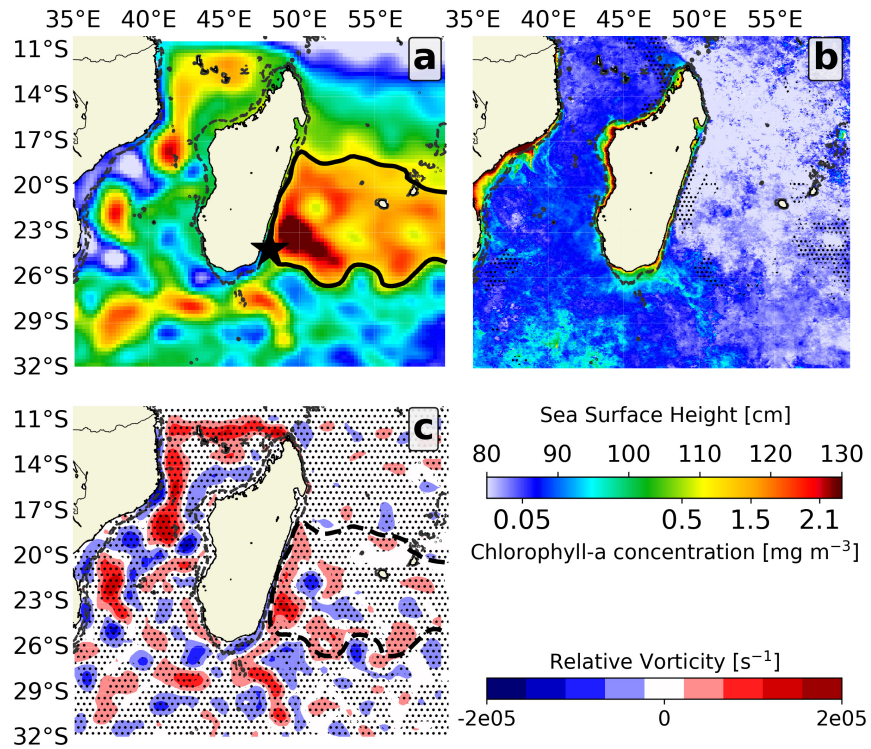


Figure 7. Spatial evidence of EMC early retroflection. (a) Composite of SSH for the periods of absolute EMC volume transport above the standard deviation (red plots in panel Figure 6a). The black contour and star indicate the identified mean EMC early retroflection extent. (b) Composites of chlorophyll-a concentration and (c) relative vorticity for the same early retroflection periods. Hatched black dots indicate a 95% confidence level according to a two-tailed Student's t-test.

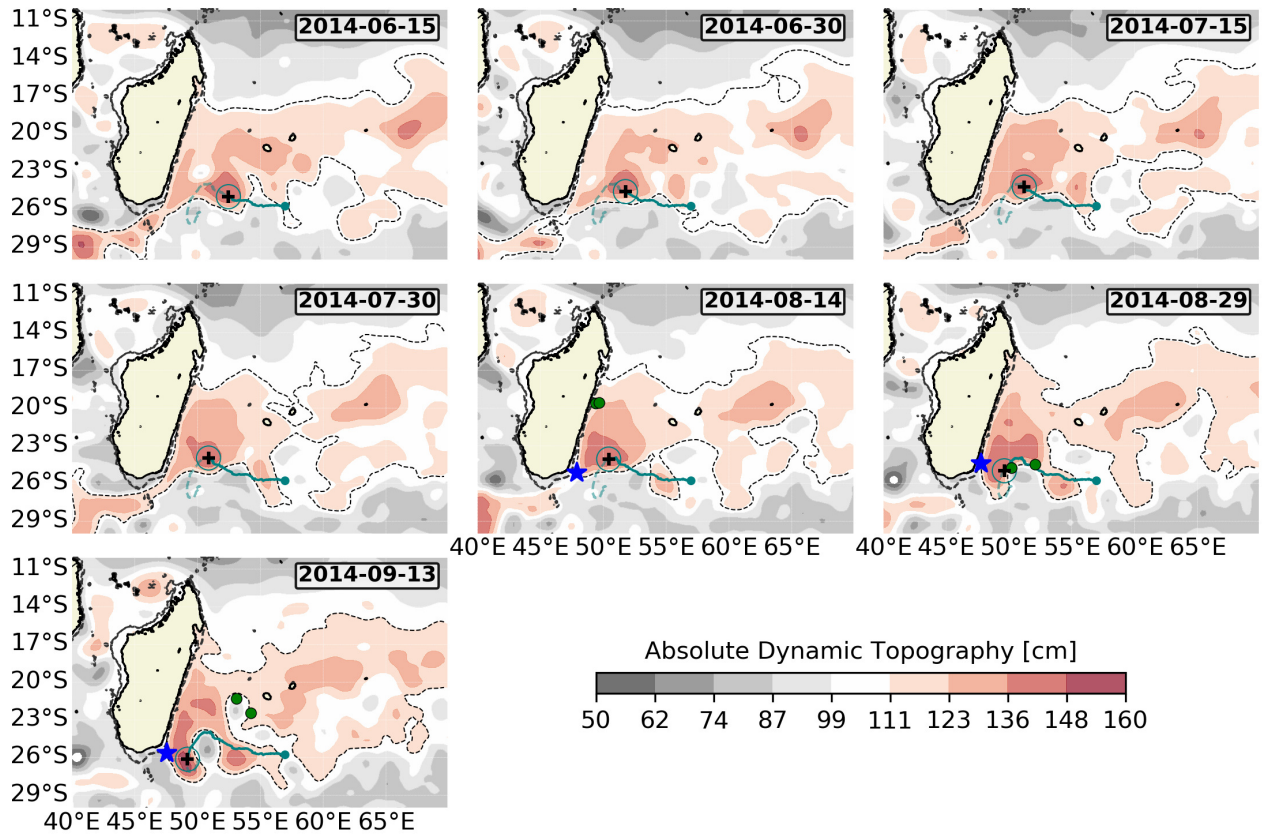


Figure 8. Synoptic development of EMC early retroflexion from onset to full formation during the period of June 20 to September 13, 2014. Blue stars are the retroflexion positioned, while the dotted black lines delineate the streamline of the flow. Maps in the background are the surface sea level at fifteen-day intervals from the period mentioned above. For all panels, the dark-cyan line represents the path of tracked anticyclonic eddies triggering early retroflexion from the automated eddy-tracking product (Mason et al., 2014). The dot in dark cyan pins the location where the eddy was formed. The black cross surrounded by a circle denotes the progressive location of the tracked anticyclonic eddy. Green dots illustrate the released virtual particles to coincide with the full development of early retroflexion. Virtual particles were released inside the EMC core, 50°E and 18°S, advected forward in time using velocity components derived from gridded altimetry products.

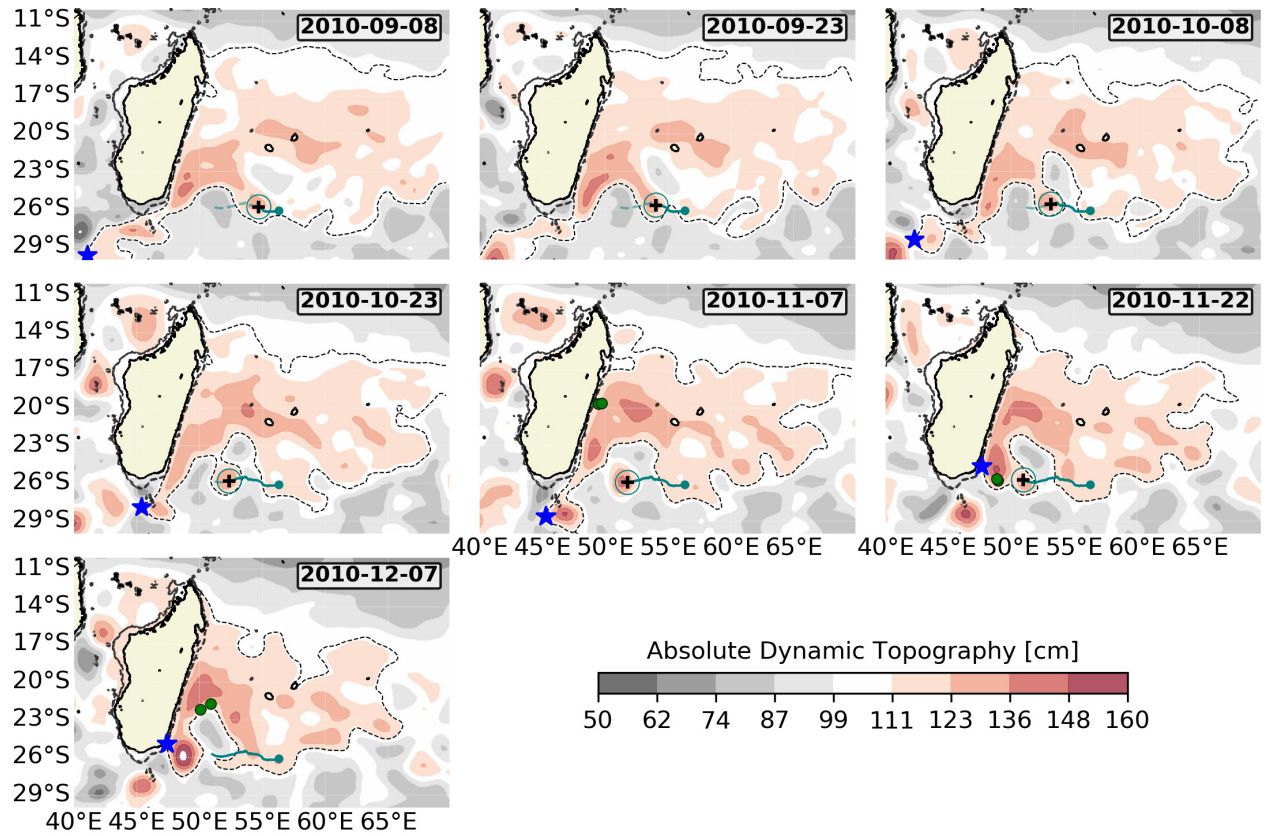


Figure 9. Synoptic development of EMC early retroreflection from onset to full formation during the period of August 27 to December 7, 2010. Same description as in Figure 8.

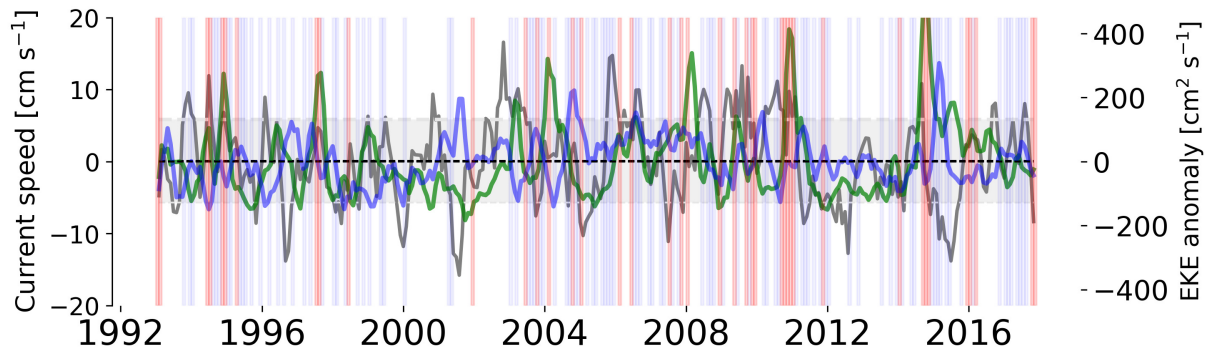


Figure 10. Dynamic processes associated with EMC retroreflection cases. Grey time series is the monthly surface current speed anomalies of the EMC from the satellite altimetry. Time series was extracted at the same location of the moored ADCP used in Figure 5b. The grey shaded area delimits the time series standard deviation. The green (blue) time series presents the EKE extracted from the green (blue) box in Figure 11a and b. All signals are filtered using a three-month running mean. The red- and blue-coloured bands indicate the EMC early retroreflection and canonical retroreflection events, respectively.

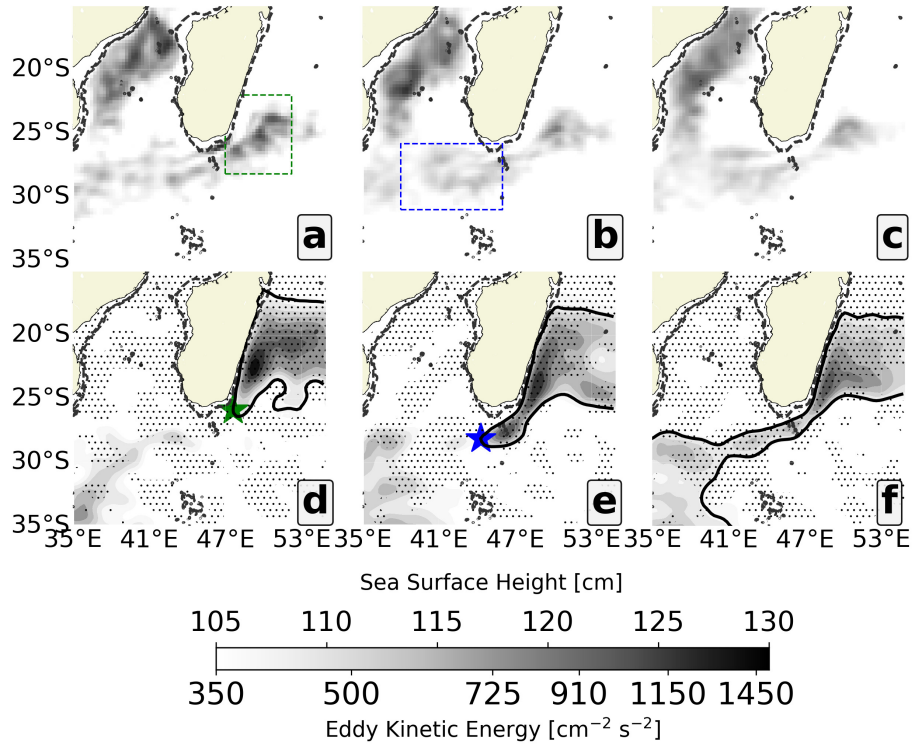


Figure 11. EMC velocity and EKE determining retroreflection position. (a), (b), and (c) are composites of EKE occurring during each retroreflection case. (d) is the composite of the SSH when the EMC surface speeds and the EKE (green box in (a)) are abnormally higher, i.e., above the first standard deviation. (e) is the SSH composite corresponding to the period of weaker EMC surface speeds, below the standard deviation, but with a high EKE (blue box in (b)). (f) is built from the composite of the period associated with weaker EKE for both green and blue boxes in (a) and (b). For (d) and (e), green and blue stars represent the EMC retroreflection positions. Hatched black dots indicate a 95% confidence level according to a two-tailed Student's t-test.

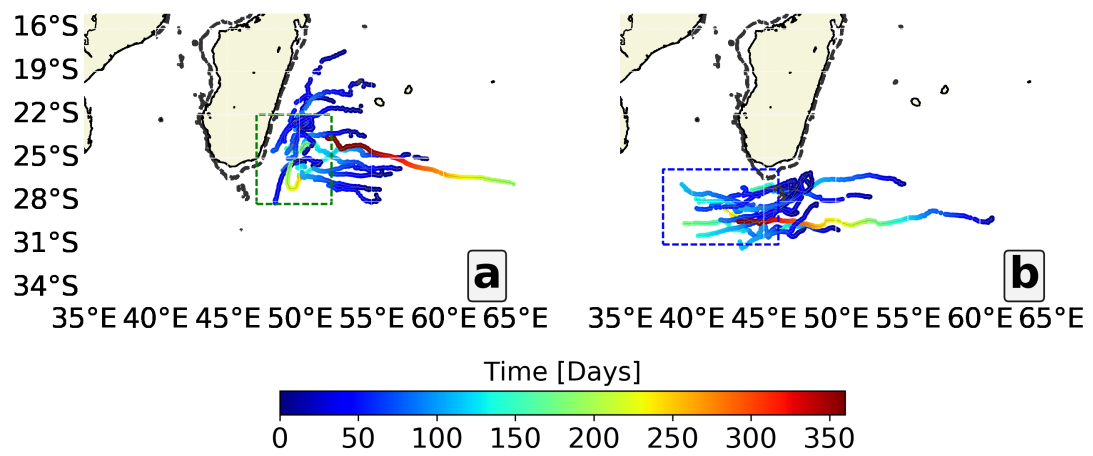


Figure 12. Anticyclonic eddies congregating in the retroflection areas. Panel (a) shows anticyclonic eddy trajectories drifting from the Indian Ocean into the green box defined in Figure 11 a. Panel (b) also shows anticyclonic eddies that come from the east concentrating in the high EKE area identified in the blue box seen in Figure 11 b.

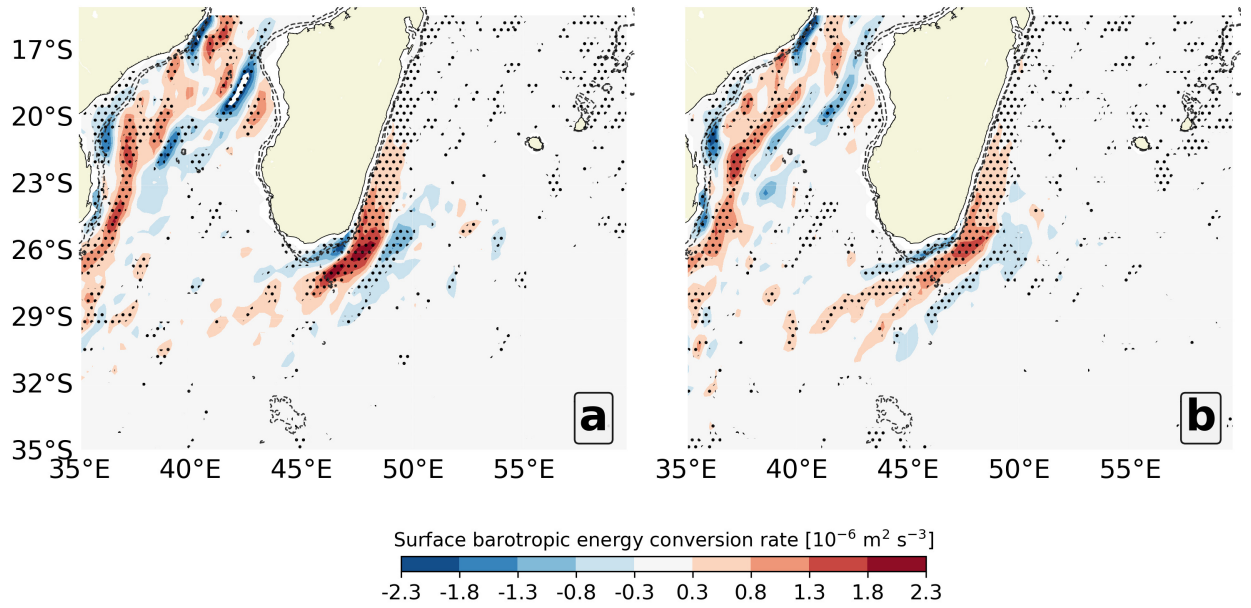


Figure 13. Transfer of kinetic energy between mesoscale eddies and the mean flow. (a) presents the surface barotropic energy conversion rate during the period of both retroreflections, early retroreflection and canonical retroreflection. (b) surface barotropic energy conversion rate during the no retroreflection period. A negative (positive) sign means that the direction of the transfer goes from the eddy field (mean flow) to the mean flow (eddy field) (Ma & Wang, 2014; R. Raj et al., 2016). Hatched black dots indicate a 95% confidence level according to a two-tailed Student's t-test.

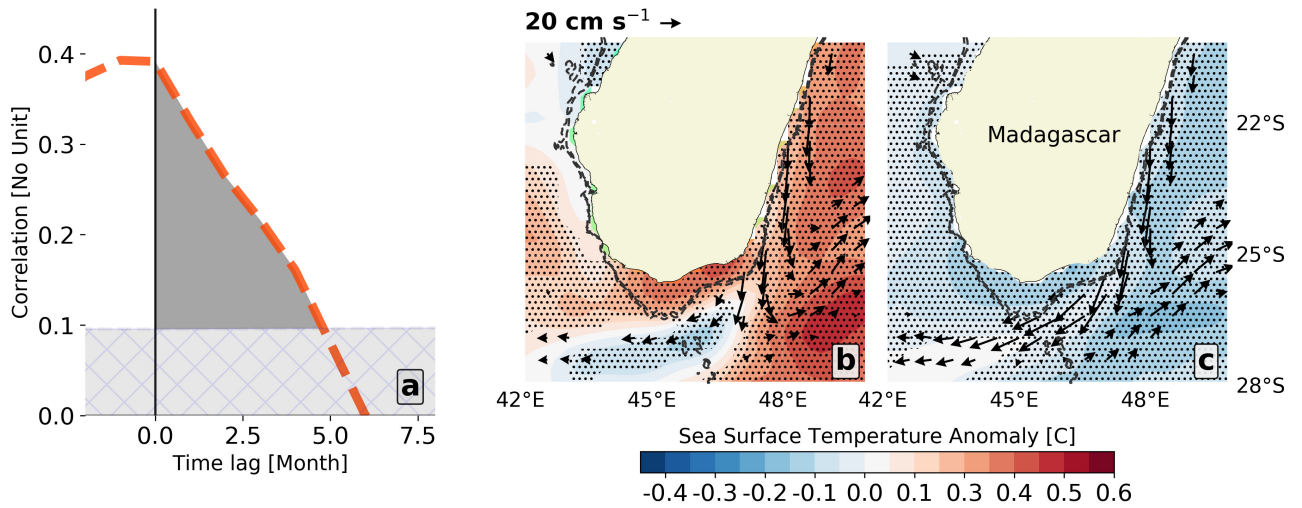


Figure 14. Impact of the EMC retroflection on coastal upwelling. (a) Lag correlation between the longitudinal EMC retroflection positions and the coastal upwelling surface temperature anomalies (Ramanantsoa et al., 2018a). (b) shows a composite period of the SST anomaly during early retroflection events. Arrows depict surface geostrophic currents and stating the early retroflection flow. Similarly, (c) represents a composite period of the SST anomaly during canonical and no retroflection events. Circles in b (red) and c (blue) emphasize the SST anomalies in the upwelling cell area. For both (b) and (c), only surface currents above 10 cm s^{-1} are shown. Hatched black dots indicate a 95% confidence level according to a two-tailed Student's t-test.

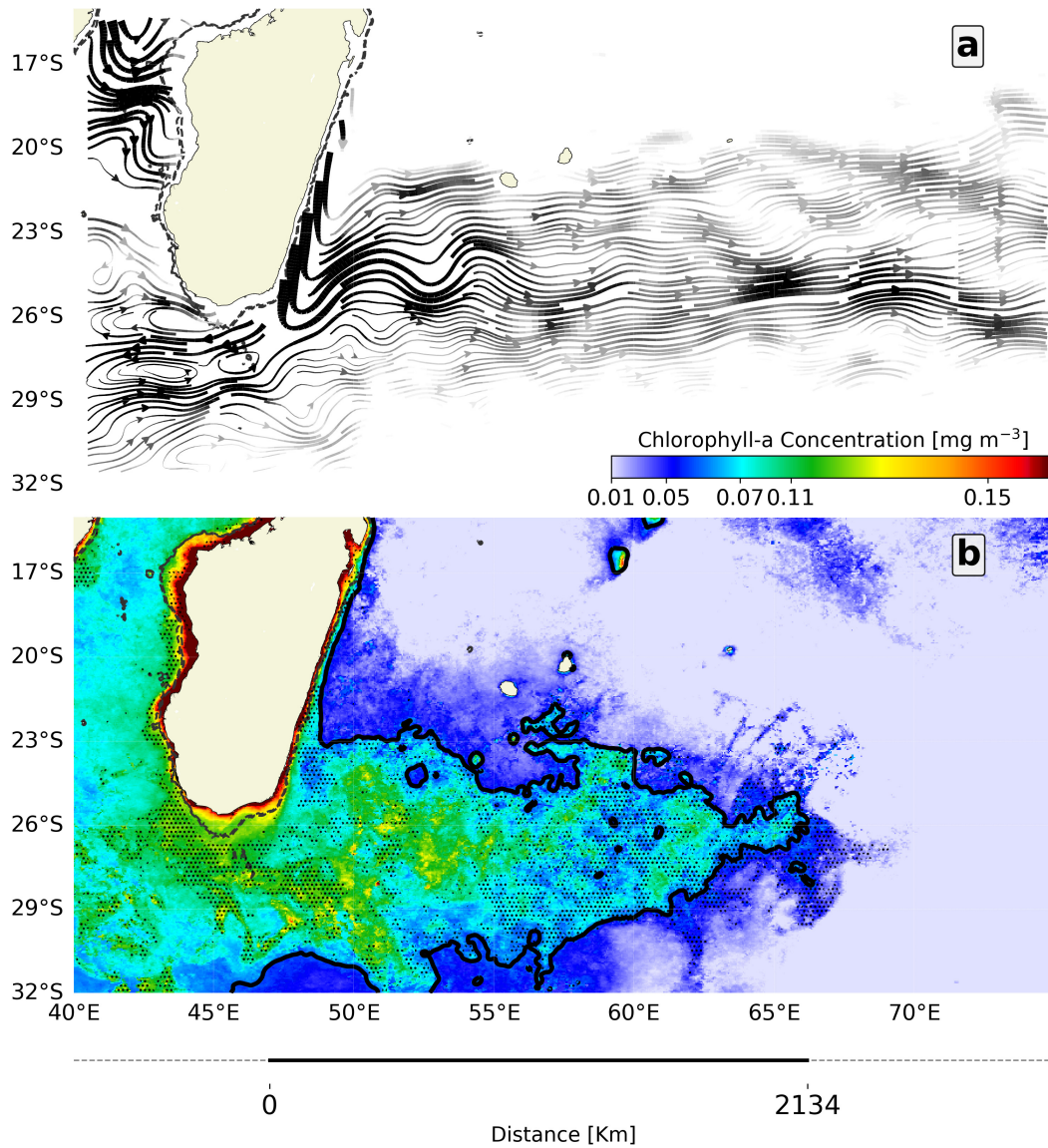


Figure 15. Connection between the EMC retroflection and the southeast Madagascar phytoplankton bloom. (a) Composite period of surface current directions during the EMC early retroflection periods. Only current speeds above 10 cm s^{-1} are shown. (b) Composite period of chlorophyll-a concentration during the periods of EMC early retroflection occurrences in austral summer. Contour depicts the 0.07 mg m^{-3} chlorophyll-a concentration in line with Dilmahamod et al. (2019). Hatched black dots indicate a 95% confidence level according to a two-tailed Student's *t*-test in (b), while confidence level for (a) has been done in previous figures and it is not reproduced to preserve its aesthetic.

727 **References**

- 728 AbdAllah, L., & Shimshoni, I. (2016). k-means over incomplete datasets using mean
 729 euclidean distance. In *International conference on machine learning and data
 730 mining in pattern recognition* (pp. 113–127).
- 731 Anggoro, S., et al. (2017). The dynamics of sea surface height and geostrophic cur-
 732 rent in the arafura sea. In *Iop conference series: Earth and environmental sci-
 733 ence* (Vol. 55, p. 012046).
- 734 Arruda, W., Zharkov, V., Deremble, B., Nof, D., & Chassignet, E. (2014). A new
 735 model of current retroflection applied to the westward protrusion of the agul-
 736 has current. *Journal of Physical Oceanography*, *44*(12), 3118–3138.
- 737 Backeberg, B. C., Penven, P., & Rouault, M. (2012). Impact of intensified in-
 738 dian ocean winds on mesoscale variability in the agulhas system. *Nature
 739 Climate Change*, *2*(8), 608. Retrieved from [https://doi.org/10.1038/
 740 nclimate1587](https://doi.org/10.1038/nclimate1587)
- 741 Bemiasa, J. (2009). *Dynamique des pecheries traditionnelles d’anchois, de calmars
 742 et de poulpes du sud-ouest de Madagascar: utilisation d’outils oceanographiques
 743 pour la gestion des ressources*. (Doctoral dissertation, Universite de Toliara,
 744 Madagascar). Retrieved from [http://archimer.ifremer.fr/doc/2009/
 745 these-6847.pdf](http://archimer.ifremer.fr/doc/2009/these-6847.pdf)
- 746 Braby, L., Backeberg, B. C., Anson, I., Roberts, M. J., Krug, M., & Reason, C. J.
 747 (2016). Observed eddy dissipation in the Agulhas Current. *Geophysical
 748 Research Letters*, *43*(15), 8143–8150. Retrieved from [https://doi.org/
 749 10.1002/2016GL069480](https://doi.org/10.1002/2016GL069480)
- 750 Cancet, M., Griffin, D., Cahill, M., Chapron, B., Johannessen, J., & Donlon, C.
 751 (2019). Evaluation of globcurrent surface ocean current products: A case study
 752 in australia. *Remote sensing of environment*, *220*, 71–93.
- 753 Chapman, P., Di Marco, S., Davis, R., & Coward, A. (2003). Flow at intermediate
 754 depths around madagascar based on alace float trajectories. *Deep Sea Research
 755 Part II: Topical Studies in Oceanography*, *50*(12-13), 1957–1986.
- 756 Chassignet, E. P., Hurlburt, H. E., Smedstad, O. M., Halliwell, G. R., Hogan, P. J.,
 757 Wallcraft, A. J., . . . Bleck, R. (2007). The hycom (hybrid coordinate ocean
 758 model) data assimilative system. *Journal of Marine Systems*, *65*(1-4), 60–83.
- 759 Chelton, D. B., Schlax, M. G., & Samelson, R. M. (2011). Global observations of

- 760 nonlinear mesoscale eddies. *Progress in oceanography*, *91*(2), 167–216.
- 761 Chen, Z., Wu, L., Qiu, B., Sun, S., & Jia, F. (2014). Seasonal variation of the south
762 equatorial current bifurcation off madagascar. *Journal of Physical Oceanogra-*
763 *phy*, *44*(2), 618–631.
- 764 Delepouille, A., Chelton, D., Schlax, M., Faugere, Y., & Dibarboure, G. (2018). 24
765 year mesoscale eddy trajectory atlas on aviso. In *Egu general assembly confer-*
766 *ence abstracts* (Vol. 20, p. 13690). Retrieved from [https://doi.org/10.1029/
767 2018JC014582](https://doi.org/10.1029/2018JC014582)
- 768 Deo, A., Ganer, D., & Nair, G. (2011). Tropical cyclone activity in global warming
769 scenario. *Natural Hazards*, *59*(2), 771.
- 770 de Ruijter, W. P., van Aken, H. M., Beier, E. J., Lutjeharms, J. R., Matano, R. P.,
771 & Schouten, M. W. (2004). Eddies and dipoles around South Madagas-
772 car: formation, pathways and large-scale impact. *Deep Sea Research Part I:
773 Oceanographic Research Papers*, *51*(3), 383–400. Retrieved from [https://
774 doi.org/10.1016/j.dsr.2003.10.011](https://doi.org/10.1016/j.dsr.2003.10.011) doi: 10.1016/j.dsr.2003.10.011
- 775 Dilmahamod, Aguiar-González, B., Penven, P., Reason, C., De Ruijter, W., Malan,
776 N., & Hermes, J. (2018). SIDDIES corridor: A major east-west pathway of
777 long-lived surface and subsurface eddies crossing the subtropical South Indian
778 Ocean. *Journal of Geophysical Research: Oceans*, *123*(8), 5406–5425.
- 779 Dilmahamod, Penven, P., Aguiar-González, B., Reason, C., & Hermes, J. (2019).
780 A new definition of the South-East Madagascar bloom and analysis of its
781 variability. *Journal of Geophysical Research: Oceans*, *124*(3), 1717–1735.
782 Retrieved from <https://doi.org/10.1029/2018JC014582>
- 783 Ducet, N., Le Traon, P.-Y., & Reverdin, G. (2000). Global high-resolution mapping
784 of ocean circulation from topex/poseidon and ers-1 and-2. *Journal of Geophys-*
785 *ical Research: Oceans*, *105*(C8), 19477–19498.
- 786 Feng, M., Weller, E., & Hill, K. (2009). The leeuwin current.
- 787 Feng, M., Zhang, N., Liu, Q., & Wijffels, S. (2018). The indonesian throughflow, its
788 variability and centennial change. *Geoscience Letters*, *5*(1), 1–10.
- 789 Gordon, A. L., Ma, S., Olson, D. B., Hacker, P., Ffield, A., Talley, L. D., ...
790 Baringer, M. (1997). Advection and diffusion of indonesian throughflow
791 water within the indian ocean south equatorial current. *Geophysical Research
792 Letters*, *24*(21), 2573–2576.

- 793 Gwilliam, C., Coward, A., De Cuevas, B., Webb, D., Rourke, E., Thompson, S.,
 794 & Döös, K. (1997). The occam global ocean model. In *Proceedings of the*
 795 *second unam-cray supercomputing conference: Numerical simulations in the*
 796 *environmental and earth sciences* (pp. 24–30).
- 797 Halo, I., Backeberg, B., Penven, P., Ansorge, I., Reason, C., & Ullgren, J. (2014).
 798 Eddy properties in the Mozambique Channel: A comparison between obser-
 799 vations and two numerical ocean circulation models. *Deep Sea Research Part*
 800 *II: Topical Studies in Oceanography*, *100*, 38–53. Retrieved from [https://](https://doi.org/10.1016/j.dsr2.2013.10.015)
 801 doi.org/10.1016/j.dsr2.2013.10.015 doi: 10.1016/j.dsr2.2013.10.015
- 802 Hartigan, J. A., & Wong, M. A. (1979). Ak-means clustering algorithm. *Journal of*
 803 *the Royal Statistical Society: Series C (Applied Statistics)*, *28*(1), 100–108.
- 804 Hastenrath, S. (2000). Zonal circulations over the equatorial indian ocean. *Journal*
 805 *of Climate*, *13*(15), 2746–2756.
- 806 Ho, C.-R., Zheng, Q., & Kuo, N.-J. (2004). Seawifs observations of upwelling south
 807 of madagascar: long-term variability and interaction with east madagascar
 808 current. *Deep Sea Research Part II: Topical Studies in Oceanography*, *51*(1-3),
 809 59–67.
- 810 Hu, S., & Fedorov, A. V. (2019). Indian ocean warming can strengthen the atlantic
 811 meridional overturning circulation. *Nature climate change*, *9*(10), 747–751.
- 812 Jia, F., Wu, L., Lan, J., & Qiu, B. (2011). Interannual modulation of eddy kinetic
 813 energy in the southeast indian ocean by southern annular mode. *Journal of*
 814 *Geophysical Research: Oceans*, *116*(C2).
- 815 Johannessen, J., Chapron, B., Collard, F., Rio, M., Piollé, J., Gaultier, L., ... others
 816 (2016). Globcurrent: Multisensor synergy for surface current estimation..
- 817 Jose, Y. S., Penven, P., Aumont, O., Machu, E., Moloney, C., Shillington, F., &
 818 Maury, O. (2016). Suppressing and enhancing effects of mesoscale dynamics on
 819 biological production in the mozambique channel. *Journal of Marine Systems*,
 820 *158*, 129–139.
- 821 Lambert, E., Bars, D. L., & de Ruijter, W. P. (2016). The connection of the indone-
 822 sian throughflow, south indian ocean countercurrent and the leeuwin current.
 823 *Ocean Science*, *12*(3), 771–780.
- 824 Laxenaire, R., Speich, S., & Stegner, A. (2020). Agulhas ring heat content and
 825 transport in the south atlantic estimated by combining satellite altimetry and

- 826 argo profiling floats data. *Journal of Geophysical Research: Oceans*, 125(9),
827 e2019JC015511.
- 828 Liu, Y., Weisberg, R. H., Vignudelli, S., & Mitchum, G. T. (2014). Evaluation of
829 altimetry-derived surface current products using lagrangian drifter trajec-
830 tories in the eastern gulf of mexico. *Journal of Geophysical Research: Oceans*,
831 119(5), 2827–2842.
- 832 Longhurst, A. (2001). A major seasonal phytoplankton bloom in the Madagas-
833 car basin. *Deep Sea Research Part I: Oceanographic Research Papers*, 48(11),
834 2413–2422. Retrieved from [https://doi.org/10.1016/S0967-0637\(01\)00024-3](https://doi.org/10.1016/S0967-0637(01)00024-3)
835 doi: 10.1016/S0967-0637(01)00024-3
- 836 Loveday, B. R., Durgadoo, J. V., Reason, C. J., Biastoch, A., & Penven, P. (2014).
837 Decoupling of the agulhas leakage from the Agulhas Current. *Journal of Phys-
838 ical Oceanography*, 44(7), 1776–1797.
- 839 Lumpkin, R., Maximenko, N., & Pazos, M. (2012). Evaluating where and why
840 drifters die. *Journal of Atmospheric and Oceanic Technology*, 29(2), 300–308.
- 841 Lumpkin, R., & Pazos, M. (2007). Measuring surface currents with surface velocity
842 program drifters: the instrument, its data, and some recent results. *Lagrangian
843 analysis and prediction of coastal and ocean dynamics*, 39–67.
- 844 Lutjeharms, J. (1976). The agulhas current system during the northeast monsoon
845 season. *Journal of Physical Oceanography*, 6(5), 665–670.
- 846 Lutjeharms, J. (1988). Remote sensing corroboration of retroflexion of the east
847 Madagascar current. *Deep Sea Research Part A. Oceanographic Research
848 Papers*, 35(12), 2045–2050. Retrieved from [https://doi.org/10.1016/
849 0198-0149\(88\)90124-0](https://doi.org/10.1016/0198-0149(88)90124-0)
- 850 Lutjeharms, J., Bang, N., & Duncan, C. (1981). Characteristics of the currents
851 east and south of Madagascar. *Deep Sea Research Part A. Oceanographic Re-
852 search Papers*, 28(9), 879–899. Retrieved from [https://doi.org/10.1016/
853 0198-0149\(81\)90008-X](https://doi.org/10.1016/0198-0149(81)90008-X)
- 854 Lutjeharms, J., & Van Ballegooyen, R. (1988). The retroflexion of the agulhas cur-
855 rent. *Journal of Physical Oceanography*, 18(11), 1570–1583.
- 856 Lutjeharms, J. R. (2006). *The agulhas current* (Vol. 329). Springer.
- 857 Ma, L., & Wang, Q. (2014). Interannual variations in energy conversion and interac-
858 tion between the mesoscale eddy field and mean flow in the kuroshio south of

- 859 japan. *Chinese Journal of Oceanology and Limnology*, *32*(1), 210–222.
- 860 Mason, E., Pascual, A., & McWilliams, J. C. (2014). A new sea surface height–
861 based code for oceanic mesoscale eddy tracking. *Journal of Atmospheric and*
862 *Oceanic Technology*, *31*(5), 1181–1188. Retrieved from [https://doi.org/10](https://doi.org/10.1175/JTECH-D-14-00019.1)
863 [.1175/JTECH-D-14-00019.1](https://doi.org/10.1175/JTECH-D-14-00019.1)
- 864 Maximenko, N., Hafner, J., & Niiler, P. (2012). Pathways of marine debris derived
865 from trajectories of lagrangian drifters. *Marine pollution bulletin*, *65*(1-3), 51–
866 62.
- 867 Menezes, V. V., Phillips, H. E., Schiller, A., Bindoff, N. L., Domingues, C. M., &
868 Vianna, M. L. (2014). South indian countercurrent and associated fronts.
869 *Journal of Geophysical Research: Oceans*, *119*(10), 6763–6791.
- 870 Menezes, V. V., Phillips, H. E., Vianna, M. L., & Bindoff, N. L. (2016). Interan-
871 nual variability of the south indian countercurrent. *Journal of Geophysical Re-*
872 *search: Oceans*, *121*(5), 3465–3487.
- 873 Menezes, V. V., & Vianna, M. L. (2019). Quasi-biennial rossby and kelvin waves in
874 the south indian ocean: Tropical and subtropical modes and the indian ocean
875 dipole. *Deep Sea Research Part II: Topical Studies in Oceanography*, *166*,
876 43–63.
- 877 Nauw, J., Van Aken, H., Lutjeharms, J., & De Ruijter, W. (2006). Intrathermocline
878 eddies in the southern indian ocean. *Journal of Geophysical Research: Oceans*,
879 *111*(C3). Retrieved from <https://doi.org/10.1029/2005JC002917>
- 880 Nauw, J., Van Aken, H., Webb, A., Lutjeharms, J., & De Ruijter, W. (2008). Ob-
881 servations of the southern East Madagascar Current and undercurrent and
882 countercurrent system. *Journal of Geophysical Research: Oceans*, *113*(C8).
883 Retrieved from <https://doi.org/10.1029/2007JC004639>
- 884 Niiler, P. (2001). The world ocean surface circulation. In *International geophysics*
885 (Vol. 77, pp. 193–204). Elsevier.
- 886 Olson, D. B., & Evans, R. H. (1986). Rings of the agulhas current. *Deep Sea Re-*
887 *search Part A. Oceanographic Research Papers*, *33*(1), 27–42.
- 888 Ou, H. W., & De Ruijter, W. P. (1986). Separation of an inertial boundary cur-
889 rent from a curved coastline. *Journal of Physical Oceanography*, *16*(2), 280–
890 289. Retrieved from [https://doi.org/10.1175/1520-0485\(1986\)016<0280:](https://doi.org/10.1175/1520-0485(1986)016<0280:SOAIBC>2.0.CO;2)
891 [SOAIBC>2.0.CO;2](https://doi.org/10.1175/1520-0485(1986)016<0280:SOAIBC>2.0.CO;2)

- 892 Palastanga, V., Van Leeuwen, P., & De Ruijter, W. (2006). A link between low-
 893 frequency mesoscale eddy variability around Madagascar and the large-scale
 894 Indian Ocean variability. *Journal of Geophysical Research: Oceans*, *111*(C9).
 895 Retrieved from <https://doi-org/10.1029/2005JC003081>
- 896 Palastanga, V., Van Leeuwen, P., Schouten, M., & De Ruijter, W. (2007). Flow
 897 structure and variability in the subtropical Indian Ocean: Instability of the
 898 south Indian Ocean Countercurrent. *Journal of Geophysical Research: Oceans*,
 899 *112*(C1). Retrieved from <https://doi-org/10.1029/2005JC003395>
- 900 Penven, P., Debreu, L., Marchesiello, P., & McWilliams, J. C. (2006). Evalua-
 901 tion and application of the roms 1-way embedding procedure to the central
 902 california upwelling system. *Ocean Modelling*, *12*(1-2), 157–187.
- 903 Penven, P., Lutjeharms, J., & Florenchie, P. (2006). Madagascar: A pacemaker for
 904 the Agulhas Current system? *Geophysical Research Letters*, *33*(17). Retrieved
 905 from <https://doi.org/10.1029/2006GL026854>
- 906 Ponsoni, L., Aguiar-González, B., Maas, L., van Aken, H., & Ridderinkhof, H.
 907 (2015). Long-term observations of the east Madagascar undercurrent. *Deep Sea*
 908 *Research Part I: Oceanographic Research Papers*, *100*, 64–78. Retrieved from
 909 <https://doi.org/10.1016/j.dsr.2015.02.004>
- 910 Ponsoni, L., Aguiar-Gonzalez, B., Nauw, J. J., Ridderinkhof, H., & Maas, L. R.
 911 (2015). First observational evidence of a north madagascar undercurrent.
 912 *Dynamics of atmospheres and oceans*, *72*, 12–20.
- 913 Ponsoni, L., Aguiar-González, B., Ridderinkhof, H., & Maas, L. R. (2016). The
 914 east madagascar current: Volume transport and variability based on long-term
 915 observations. *Journal of Physical Oceanography*, *46*(4), 1045–1065.
- 916 Quartly, G. D., Buck, J. J., Srokosz, M. A., & Coward, A. C. (2006). Eddies around
 917 Madagascar-The retroflection re-considered. *Journal of Marine Systems*, *63*(3),
 918 115–129. Retrieved from <https://doi.org/10.1016/j.jmarsys.2006.06.001>
 919 doi: j.jmarsys.2006.06.001
- 920 Quartly, G. D., & Srokosz, M. A. (2002). Satellite observations of the agulhas cur-
 921 rent system. *Philosophical Transactions of the Royal Society of London. Series*
 922 *A: Mathematical, Physical and Engineering Sciences*, *361*(1802), 51–56. Re-
 923 trieved from <https://doi.org/10.1098/rsta.2002.1107>
- 924 Raj, R., Johannessen, J., Eldevik, T., Nilsen, J. Ø., & Halo, I. (2016). Quanti-

- 925 fying mesoscale eddies in the lofoten basin. *Journal of Geophysical Research:*
926 *Oceans*, 121(7), 4503–4521.
- 927 Raj, R. P., Peter, B. N., & Pushpadas, D. (2010). Oceanic and atmospheric
928 influences on the variability of phytoplankton bloom in the southwest-
929 ern Indian Ocean. *Journal of Marine Systems*, 82(4), 217–229. Re-
930 trieved from <https://doi.org/10.1016/j.jmarsys.2010.05.009> doi:
931 10.1016/j.jmarsys.2010.05.009
- 932 Ramanantsoa. (2018b). *Variability of coastal upwelling south of madagas-*
933 *car* (Doctoral dissertation, University of Cape Town). Retrieved from
934 <https://open.uct.ac.za/handle/11427/29859>
- 935 Ramanantsoa, Krug, M., Penven, P., Rouault, M., & Gula, J. (2018a). Coastal
936 upwelling south of Madagascar: Temporal and spatial variability. *Journal of*
937 *Marine Systems*, 178, 29–37. Retrieved from [https://doi.org/10.1016/](https://doi.org/10.1016/j.jmarsys.2017.10.005)
938 [j.jmarsys.2017.10.005](https://doi.org/10.1016/j.jmarsys.2017.10.005)
- 939 Ramanantsoa, J. D., Penven, P., Krug, M., Gula, J., & Rouault, M. (2018). Un-
940 covering a new current: The southwest madagascar coastal current. *Geophysi-*
941 *cal Research Letters*, 45(4), 1930–1938.
- 942 Rao, S. A., Dhakate, A. R., Saha, S. K., Mahapatra, S., Chaudhari, H. S., Pokhrel,
943 S., & Sahu, S. K. (2012). Why is indian ocean warming consistently? *Climatic*
944 *change*, 110(3), 709–719.
- 945 Renault, L., McWilliams, J. C., & Penven, P. (2017). Modulation of the Agulhas
946 Current retroflection and leakage by oceanic current interaction with the at-
947 mosphere in coupled simulations. *Journal of Physical Oceanography*, 47(8),
948 2077–2100. Retrieved from <https://doi.org/10.1175/JPO-D-16-0168.1>
- 949 Reynolds, R. W., Smith, T. M., Liu, C., Chelton, D. B., Casey, K. S., & Schlax,
950 M. G. (2007). Daily high-resolution-blended analyses for sea surface tempera-
951 ture. *Journal of climate*, 20(22), 5473–5496.
- 952 Ridderinkhof, W., Le Bars, D., Von der Heydt, A., & De Ruijter, W. (2013). Dipoles
953 of the south east madagascar current. *Geophysical Research Letters*, 40(3),
954 558–562.
- 955 Rio, M.-H., & Santoleri, R. (2018). Improved global surface currents from the merg-
956 ing of altimetry and sea surface temperature data. *Remote sensing of Environ-*
957 *ment*, 216, 770–785.

- 958 Saji, N., Goswami, B., Vinayachandran, P., & Yamagata, T. (1999). A dipole mode
959 in the tropical indian ocean. *Nature*, *401*(6751), 360–363.
- 960 Saunders, P. M., Coward, A. C., & de Cuevas, B. A. (1999). Circulation of the
961 pacific ocean seen in a global ocean model: Ocean circulation and climate ad-
962 vanced modelling project (occam). *Journal of Geophysical Research: Oceans*,
963 *104*(C8), 18281–18299.
- 964 Schlax, M. G., & Chelton, D. B. (2016). The "growing method" of eddy identifi-
965 cation and tracking in two and three dimensions. *College of Earth, Ocean and*
966 *Atmospheric Sciences, Oregon State University, Corvallis, Oregon*, 8.
- 967 Schott, F. A., Xie, S.-P., & McCreary Jr, J. P. (2009). Indian ocean circulation and
968 climate variability. *Reviews of Geophysics*, *47*(1).
- 969 Schouten, M. W., De Ruijter, W. P., & Van Leeuwen, P. J. (2002). Upstream
970 control of agulhas ring shedding. *Journal of Geophysical Research: Oceans*,
971 *107*(C8), 23–1. Retrieved from <https://doi.org/10.1098/rsta.2004.1478>
- 972 Schouten, M. W., de Ruijter, W. P., Van Leeuwen, P. J., & Ridderinkhof, H. (2003).
973 Eddies and variability in the Mozambique Channel. *Deep Sea Research Part*
974 *II: Topical Studies in Oceanography*, *50*(12-13), 1987–2003. Retrieved from
975 [https://doi.org/10.1016/S0967-0645\(03\)00042-0](https://doi.org/10.1016/S0967-0645(03)00042-0)
- 976 Sheppard, C. R. (2003). Predicted recurrences of mass coral mortality in the indian
977 ocean. *Nature*, *425*(6955), 294–297.
- 978 Siedler, G., Rouault, M., Biastoch, A., Backeberg, B., Reason, C. J., & Lutjeharms,
979 J. R. (2009). Modes of the southern extension of the east Madagascar cur-
980 rent. *Journal of Geophysical Research: Oceans*, *114*(C1). Retrieved from
981 <https://doi.org/10.1029/2008JC004921> doi: 10.1029/2008JC004921
- 982 Siedler, G., Rouault, M., & Lutjeharms, J. R. (2006). Structure and origin of the
983 subtropical South Indian Ocean Countercurrent. *Geophysical Research Letters*,
984 *33*(24). Retrieved from <https://doi.org/10.1029/2006GL027399>
- 985 Singh, A., Yadav, A., & Rana, A. (2013). K-means with three different distance
986 metrics. *International Journal of Computer Applications*, *67*(10).
- 987 Sprintall, J., Chong, J., Syamsudin, F., Morawitz, W., Hautala, S., Bray, N., & Wi-
988 jffels, S. (1999). Dynamics of the south java current in the indo-australian
989 basin. *Geophysical Research Letters*, *26*(16), 2493–2496.
- 990 Sprintall, J., Wijffels, S. E., Molcard, R., & Jaya, I. (2009). Direct estimates of the

- 991 indonesian throughflow entering the indian ocean: 2004–2006. *Journal of Geo-*
992 *physical Research: Oceans*, 114(C7).
- 993 Srokosz, M., Robinson, J., McGrain, H., Popova, E., & Yool, A. (2015). Could the
994 madagascar bloom be fertilized by madagascan iron? *Journal of Geophysical*
995 *Research: Oceans*, 120(8), 5790–5803.
- 996 Swallow, J., Fieux, M., & Schott, F. (1988). The boundary currents east and north
997 of madagascar: 1. geostrophic currents and transports. *Journal of Geophysical*
998 *Research: Oceans*, 93(C5), 4951–4962.
- 999 Swallow, J. C., Schott, F., & Fieux, M. (1991). Structure and transport of the east
1000 african coastal current. *Journal of Geophysical Research: Oceans*, 96(C12),
1001 22245–22257.
- 1002 Talley, L. D. (2013). Closure of the global overturning circulation through the in-
1003 dian, Pacific, and southern oceans: Schematics and transports. *Oceanography*,
1004 26(1), 80–97. Retrieved from <http://www.jstor.org/stable/24862019>
- 1005 Ternon, J.-F., Roberts, M., Morris, T., Hancke, L., & Backeberg, B. (2014). In situ
1006 measured current structures of the eddy field in the mozambique channel. *Deep*
1007 *Sea Research Part II: Topical Studies in Oceanography*, 100, 10–26.
- 1008 van Sebille, E., Biastoch, A., Van Leeuwen, P., & De Ruijter, W. (2009). A weaker
1009 Agulhas Current leads to more Agulhas leakage. *Geophysical Research Letters*,
1010 36(3). Retrieved from <https://doi.org/10.1029/2008GL036614>
- 1011 White, C., Selkoe, K. A., Watson, J., Siegel, D. A., Zacherl, D. C., & Toonen, R. J.
1012 (2010). Ocean currents help explain population genetic structure. *Proceedings*
1013 *of the Royal Society B: Biological Sciences*, 277(1688), 1685–1694.
- 1014 Wyrтки, K. (1973). Physical oceanography of the indian ocean. In *The biology of the*
1015 *indian ocean* (pp. 18–36). Springer.
- 1016 Ye, J., Zhao, Z., & Liu, H. (2007). Adaptive distance metric learning for clustering.
1017 In *2007 ieee conference on computer vision and pattern recognition* (pp. 1–7).